Title

I. STABILITY RANGE OF MOC (HP2) II. THERMODYNAM1C PROPERTIES OF GENERALIZED LEWIS ACID-BASE INTERMETALL1CS

Author

Kouvetakis, J.

Publication Date

1988-05-01

Lawrence Berkeley Laboratory
UNIVERSITY OF CALIFORNIA

Materials & Chemical Sciences Division

I. Stability Range of MoC (hP2)

II. Thermodynamic Properties of Generalized Lewis Acid-Base Intermetallics

J. Kouvetakis
(Ph.D. Thesis)

May 1988

Prepared for the U.S. Department of Energy under Contract Number DE-AC03-76SF00098.

DISCLAIMER

LBL-25340

I. Stability Range of MoC (hP2)
II. Thermodynamic Properties of Generalized Lewis Acid-Base Intermetallics

John Kouvetakis

(Ph.D. thesis)

Lawrence Berkeley Laboratory
University of California
Berkeley, CA 94720

May 1988

Supported by the U.S. Department of Energy under Contract Number DE-AC03-76SF00098.

I. Stability Range of MoC (hP2)

II. Thermodynamic Properties of Generalized Lewis Acid-Base Intermetallics

John Kouvetakis

ABSTRACT

PART I The γ-MoC phase with the hexagonal WC structure was prepared without the presence of metal stabilizers at temperatures below 1000 °C. This phase was found to be thermodynamically stable at low temperatures and decomposed to Mo_2C and graphite at 1400 K. Using equilibrium and thermodynamic data, the thermodynamic quantities of this phase were calculated as $S^o_{298}/R = 4.41 \pm 0.3$ and $\Delta H^o_{298}/R = -3430 \pm 800$ K.

PART II Oxide equilibration and solid-state galvanic cell experiments were used to study thermodynamic properties of binary Lewis acid-base stabilized transition metal alloys. The activity of vanadium was determined in alloys of vanadium with platinum group metals such as Rh, Pd and Ir at 1000 °C. The activities of titanium in titanium-iridium alloys and of niobium in Nb_3Ir were determined at 1400 °C. The ternary phase diagram of V-Pd-O at 1000 °C was obtained. Based on the vanadium-palladium results, a partial titration curve of palladium by vanadium was constructed. The excess partial molar Gibbs free energy of vanadium at infinite dilution was found to be -36.4 kcal mol^{-1} at 1000 °C. The results of this study are in agreement with the predictions of Brewer's theory of transition metal alloy acid-base behavior.

To Leo Brewer and Jim Piperis.

ACKNOWLEDGEMENT

To Professor Leo Brewer, I offer my sincere thanks and deepest appreciation for his patience, warmth, kindness and support that he showed me during my years at Berkeley. I shall always be indebted and grateful to him for believing in me.

I would like to thank my mother and my wife, Ann, for their love and support. Many thanks to Professor Richard A. Andersen for his guidance and advice. I am grateful to the technical support staff of the Materials and Chemical Sciences Division of Lawrence Berkeley Laboratory and the Department of Chemistry, and particularly to John Holthuis and Tom Lawhead for providing the necessary assistance during this work. I also thank my coworkers Joe Bularzik, Mike Cima, Susan Leonard and Karen Krushwitz. A special thanks to my friends Bart Ebbinghaus, Steve Mayorga, Rika Hagiwara and Tom Richardson for their pleasant presence in the lab. Papa Manolis and the beautiful beaches of Crete will never be forgotten. "Blue skies."

This work was supported by the Director, Office of Energy Research, Office of Basic Energy Sciences, Materials Sciences Division, U.S. Dept. of Energy under contract number DE-AC03-76SF00098.

TABLE OF CONTENTS

PART 1. TEMPERATURE STABILITY RANGE OF THE BINARY MoC PHASE

I. INTRODUCTION

The study of the molybdenum carbon system was initiated by Moissan.[1] He established the existence of two phases, Mo_2C and MoC. Later reports[3-4] have confirmed the presence of MoC and Mo_2C as stable phases up to their melting points. Kuo and Hägg[2] made MoC and Mo_2C by carburizing molybdenum with carbon monoxide. Their MoC phase had the hexagonal WC structure. In addition to these phases, a γ'-MoC (TiP-type) phase was discovered in their study. A more careful and definitive study by Rudy[5-8] characterized these "MoC" phases as non-stoichiometric carbides intermediate in composition to MoC and Mo_2C. The thermodynamically stable phases that Rudy found are the hexagonal η-MoC_{1-x} with composition near Mo_3C_2 and stable above 1928 K and the α-MoC_{1-x} (NaCl-type) with composition $MoC_{.7}$ and stable above 2233 K.

In addition, Rudy reported two modifications of Mo_2C. The α-Mo_2C (Fe_2N-type) orthorhombic[9] phase and the β-Mo_2C (hP3) hexagonal phase. The currently accepted phase diagram[10-11] of molybdenum and carbon contains only these four phases (Fig. 1). The γ'-MoC phase has been found to be metastable. The γ-MoC phase with the WC structure is also considered metastable unless stabilized by impurities. Toth[12] claims that nitrogen and oxygen are the common impurities that stabilize this structure.

Ternary $MoC_{1-x}N_x$ phases, x = (0.15-1), isostructural to γ-MoC have been reported. Rudy, Schuster, and Nowotny[13] also found that small amounts of Co, W, and Fe stabilize γ-MoC. They extrapolated these data for the γ-MoC structure containing 5% Co, W, and Fe to very low concen-

trations and predicted that this phase might be stable at temperatures below 1400 K. In a later paper, Rudy et al. give a phase diagram in which MoC (hP2) is shown to be stable up to ~1450 K. However, they report that the reaction of carbon with Mo_2C to form MoC below 1450 K never occurs within feasible lengths of time.[14] This result was accepted by Brewer and Lamoreaux,[15] who included MoC as stable up to 1420 ±40 K in their phase diagram (Fig. 2).

This study was motivated by the uncertainty in the existence of the γ-MoC phase. The goal of the present work is to prepare γ-MoC free of transition metal impurities or nitrogen and oxygen, and to determine its temperature stability range.

II. EXPERIMENTAL

A. Apparatus

Several high temperature furnaces were used for the sample preparation and annealing.

1. Gradient furnace. A gradient furnace similar to the one used in the Co-Mo system[16] was used to anneal a large number of samples at different temperatures at the same time. It is made of a 38 mm outer diam. and 32 mm inner diam. and 0.9 m in length alumina tube wound with 0.5 mm kanthal wire in seven separate zones. Each zone is 102-114 mm long, and consists of equally spaced windings. The spacing of the wiring ranges from 1 mm at the first zone (hot end) to 19 mm at the last zone (cool end). These Kanthal windings were covered with an alumina-silica paste which upon drying served as an electrical insulator. This tube was mounted horizontally in a cylindrical stainless steel (0.41 m diam.) case packed with alumina wool which served as a thermal insula-

tor. The furnace operated with a 220 V power supply equipped with a Honeywell temperature controlled. The temperature inside the furnace was monitored with five platinum/rhodium (Pt 90%/Rh 10%) thermocouples which were connected to a calibrated Doric 142 trendicator which digitally displayed the temperature of each thermocouple.

2. Hot press. A hot press was used for the initial reactions of the samples. This was the first and most critical part of the experiment because the stock powders used to make the samples were consolidated by heating and pressing in one step. Intimate contact of the particles facilitates rapid diffusion and equilibration in a reasonable amount of time. This instrument was designed and built at Lawrence Berkeley Laboratory and is a simple resistance furnace equipped with a pressing assembly and operated at high vacuum or under inert atmospheres. The heating element is essentially a 25 mm high and 0.2 mm thick tungsten or tantalum strip cylindrically shaped to surround the graphite die. This element was mounted on water cooled copper leads which were connected to a variable power supply. A set of molybdenum or tantalum heat shields held together by tantalum screws and separated by tantalum spacers were located concentrically to the heating element, and were supported on a graphite base. The top and bottom of this cylindrical shielding was capped by sets of circular and horizontal shields. A small opening on the top set of the horizontal shields provided passage for the graphite ram which is hydraulically driven and can apply pressures up to 2000 atm on a 13 mm graphite die. The graphite die, which is surrounded by the heating elements and the shields, is made of 99.9% ATJ high density graphite material and is 38 mm outer diam, 13 mm inner diam and 38 mm high. The pressing and heating components were based in

a 0.46 m × 0.46 m cubical chamber which was connected to a diffusion pump. The pressure inside the chamber was less than 10^{-5} torr. The maximum temperature under high vacuum was ~1800 °C. A 653 nm Leeds and Northrup optical pyrometer, calibrated according to National Bureau of Standards specifications, was used to make temperature measurements through a quartz window on the chamber. A high vacuum, tungsten mesh resistance, Brew furnace was used for long heat treatments of the samples in extremely clean environments.

3. Quenching apparatus. Some of the materials needed in this study are stable at temperatures greater than 1800 °C. For their preparation an ABAR high vacuum furnace with a tungsten mesh element and a quenching attachment was used. The quenching attachment was simply a quartz tube containing tin metal and was mounted on the bottom of the high vacuum chamber away from the heat source. The tin was externally heated to its melting point (300 °C). The samples were heated to high temperature by the heating elements and were immediately dropped in the molten tin to cool. A copper block cooled externally with liquid nitrogen was often used instead of tin to quench samples.

4. X-ray. X-ray diffraction was performed on a Siemens D-500 diffractometer using CuKα radiation, and graphite monochrometer. A step-scan mode was used to collect data every 0.1°/second, or 0.03° for two or three second periods. The data were immediately recorded by a computer which provided a 2θ versus intensity plot with the d-spacing and the average number of counts of each reflection. The computer memory contained the entire and current JCPDS-files. At any time, any x-ray pattern from the JCPDS could be recalled and compared to the pattern of the sample under examination.

5. Vacuum line. A metal vacuum line was used to handle the dry bromine catalyst or to seal samples in quartz tubes under vacuum or an inert atmosphere. This line was constructed with pieces of 6 mm outer diam. stainless steel tubing interconnected with Swagelock fitting teflon ferrules, and Whitey stainless steel valves with teflon tipped stems. The line was equipped with an Helicoid 2 atm pressure gauge, calibrated in 5 torr intervals. The system was pumped by a mechanical pump to 30 millitorr through a liquid nitrogen cooled Pyrex trap.

B. Sample Preparation

The desired amounts of stock powders were weighed inside glass vials that had been previously washed, rinsed with acetone and dried. The powders were mixed with Pyrex mixing balls and were rotated in a rotary mixer for 5-6 h. The resulting mixture was then ground with a mortar and pestle for 10-15 min to assure intimate contact of the particles. The mixture was pressed into pellets in a 13 mm steel die at 670 atm for 5 min. The compressed pellets were scraped with a glass slide to remove any possible contamination from the die and were hot pressed at 1300 °C and 330 atm for 15 min or until constant pressure in the sample was achieved. A micro-pressure meter measured the pressure variation inside the reaction die. A good indication that the reaction was completed and sintering had occurred was a constant pressure reading on the meter. Since the samples contained carbon and molybdenum, there were side reactions with the rams of the die. The portion of the sample that contained extra carbon from the die was cut off with a diamond coated blade. The specimens were subsequently annealed under high vacuum, 10^{-7} torr, in the Brew furnace for 6 to 12 h at a temperature range of 1100-1800 °C, depending on which phases needed to be present.

The characterization was performed with x-ray diffraction and optical microscopy. A typical 3 to 4 g sample was sliced into 0.5 to 1 g portions with the diamond blade and were then used for the subsequent experiments.

The specimens that were treated in open furnaces or required halogen catalyst or transport agents were enclosed in sealed quartz tubes. The samples that contained high temperature phases were heat treated in the ABAR furnace and quenched on a copper plate or in a tin bath. The tin was dissolved away using nitric acid. Silicon carbide sandpaper was used to remove any possible contamination by the copper plate on the hot sample. The materials used for the sample preparation were Cerac molybdenum powder (-100 mesh, 99.98% pure) and Cerac graphite powder (-200 mesh, 99.99% pure, spectragrade). All heat treatments were preformed under high vacuum to avoid contamination of the sample by nitrogen or oxygen. A series of tantalum shields were used in the furnaces to contain the heat and to act as a getter for gaseous impurities.

III. RESULTS

A. MoC Formation and Characterization

Based on the results of Rudy et al.,[13] Brewer predicted that MoC should be stable below 1100 °C and decompose to α-Mo_2C and carbon at higher temperatures. Earlier attempts[17] to make MoC from carbon and molybdenum were not successful. Present efforts to make MoC by combining carbon and molybdenum at 50 at.% and heating the mixture at 1000 °C for several weeks also failed. Mo_2C and carbon were then combined in equimolar amounts and heated in the presence of bromine vapor in quartz ampules for nearly 2 1/2 months. The bromine was added as a catalyst or

transport agent to facilitate rapid growth of any MoC crystallites that would form by the reaction of Mo_2C and carbon. Even in the presence of the catalyst and the extremely long heat treatment MoC, was not produced by this method.

It is expected that MoC would have a narrow range of optimum rate of formation just below its disproportionation temperature which was expected[15] to be around 1400 K. A combination of slow diffusion rates and difficulty in crystallization in this system may require an unreasonable amount of time to determine just by trial and error where this range would be. Therefore a different approach had to be taken and special techniques were needed to solve the problem. A gradient furnace in which several samples can be heated at a range of temperatures simultaneously was needed to find the "best" temperature of formation in this region of stability.

It was also shown that Mo_2C would not react readily with carbon to form MoC with WC structure. It was postulated that another carbide that had a composition intermediate to that of Mo_2C and MoC, and was thermodynamically unstable at low temperatures, may disproportionate when heated below 1000 °C to Mo_2C, carbon, and MoC-seed crystals that could act as nucleating centers for further MoC growth. The next carbide to stabilize with increase in temperature is the η-MoC_{1-x}, stable only above 1655 ±15 °C. At the disproportionation temperature the η-phase has a stoichiometry of Mo_3C_2.

Samples of 50 at% Mo and 50 at% C were hot-pressed at 1200 °C and annealed at 1800 °C for 6 h. Rapid cooling at the end of 6 h yielded Mo_2C, carbon and traces of Mo_3C_2. Seven 1 g specimens listed in Table 1 were loaded in the dry box in quartz tubes that had previously been

dried and degassed under dynamic vacuum with an oxygen-methane flame. Bromine (1-2 torr), dried over P_2O_5, was transferred into the tubes via the vacuum line. The pressure of the bromine was controlled by a slush bath. The bromine was condensed and kept at the bottom of the tubes while they were sealed under vacuum with the oxygen-methane torch. The sealed ampules were tied to an alumina rod with Pt wire and inserted in the gradient furnace. The location of each ampule along the rod was measured so the temperature could be accurately measured at any time. After two weeks the samples were removed from the furnace and examined by x-ray diffraction. The MoC phase appeared in most of the samples along with Mo_2C and carbon. The diffraction pattern of the sample containing γ-MoC, Mo_2C and traces of carbon is compared with the diffraction pattern of WC in Fig. 3. The optical micrograph of a sample containing these three phases is schown in Fig. 3b. The diffraction pattern of a sample containing γ-MoC and Mo_2C is compared with a calculated pattern of Mo_2C in Fig. 3a. The d-spacings and the Miller indices for MoC and Mo_2C are listed in Tables 2 and 3. The Mo_3C_2 had indeed provided a way for MoC formation. Examination of the peak intensities indicated that the maximum MoC growth had occurred at 960 to 1000 °C. Only Mo_2C and carbon were observed above 1120 °C which was designated as the decomposition temperature of MoC.

The formation of MoC from mixtures of Mo_2C, C and Mo_3C_2 was reproduced at 975 °C with 2 torr of Br_2.

$$C + Mo_2C + Mo_3C_2 \xrightarrow[2\ days]{Br_2} MoC + Mo_2C + C$$

With increase in the amount of catalyst and length of the reaction time,

the carbon was found to react completely with Mo_2C.

$$C/Mo_2C/MoC \xrightarrow[7\ days]{7\ Torr\ Br_2} MoC + Mo_2C$$

High yields of MoC were obtained when pure quenched Mo_3C_2 was used as the starting material and in the presence of Br_2 vapors.

$$Mo_3C_2 \xrightarrow[Br_2]{975^oC} MoC + Mo_2C$$

In the presence of carbon, Mo_3C_2 again decomposed to Mo_2C and MoC.

$$Mo_3C_2 + C \xrightarrow{975^oC} MoC + Mo_2C + C$$

Pure Mo_3C_2 was prepared from hot-pressed samples that contained 40 at% C and 60 at% Mo. The samples were annealed at 1800 °C and were quenched in a tin bath. During the annealing, the sample was tied with Mo wire to a graphite disk. The more buoyant graphite facilitated the rapid emergence of the cooled sample from the tin bath to minimize contamination by the tin.

To show that bromine did not dissolve in the lattice to stabilize the MoC phase, a mixture of Mo_3C_2, Mo_2C and graphite was heated at 975 °C for 15 days with no bromine present and MoC was produced. A similar sample that contained bromine simply showed enhanced MoC growth.

Several reactions between MoO_2 and Mo_2C plus carbon were carried out at 1000 to 1100 °C to see if ternary $MoC_{1-x}O_x$ phases with the WC structure could be made. All reactions yielded mixtures of MoO_2, Mo_2C and C. At temperatures greater than 1100 °C, MoO_2 was reduced by carbon.

IV. DISCUSSION AND CONCLUSIONS

MoC cannot be made by simply reacting Mo_2C and carbon. The disproportionation of the high temperature Mo_3C_2 phase, however, yields MoC and Mo_2C. Once some MoC crystals are available, reaction of carbon with Mo_2C in the presence of a transport agent occurs. The MoC crystals provide nucleating sites for further growth. MoC is shown to be thermodynamically stable in the absence of impurity stabilizers below 1120 °C. Above this temperature it disproportionates to α-Mo_2C and carbon. A close examination of the structures of these carbides offers an explanation as to why MoC grows out of Mo_3C_2. The structure of Mo_3C_2 was solved by Nowotny, et al.[18] in 1954. It involves close-packed molybdenum atoms with the carbon occupying the interstitial positions. The sequence of Mo layers is designated as ABCACB, ABCACB. Of the available carbon sites, two-thirds are equivalent and one-third are slightly different. In the Mo_2C phase the hexagonal close-packed lattice of molybdenum is symbolized as AB,AB with all the available carbon sites equivalent and only one-half occupied. At low temperature where the entropy term is not as significant, the ABCACBA hexagonal lattice separates into two lattices, the ABAB of the Mo_2C phase and the CC of the MoC phase (Fig. 5). Although at 1650 °C Mo_3C_2 disproportionates to carbon and β-Mo_2C, when heated below 1120 °C it loses molybdenum and carbon to form MoC and α-Mo_2C. Rearrangement of the ABCACBA stacking to the ABABAB stacking without loss of molybdenum appears to be very difficult at low temperatures.

The crystal structure of elements or compounds are often correlated to their electronic configurations. For the diamond structure, 4 elec-

trons per atom are needed. A close examination of valence electron concentration of borides, carbides, nitrides, and phosphides of transition metals that have the hexagonal (hP2) WC-type structure indicates a range of 5 to 6 electrons per atom (Table 4). An optimum of 5.5 electrons per atom may be required for maximum stability. Comparison of heats of formation of MoC and MoN supports this assumption. The enthalpies of formation of γ-MoC and its structural relative MoN are $\Delta H_f^\circ/R$ = -3.40 ±0.80 kilo-Kelvin and 5.0 ±1.0 kilo-Kelvin, respectively. A Lewis acid-base type effect may contribute to the higher stability of MoN. The nitrogen may donate its nonbonding electron pair to the empty p orbitals of molybdenum. The MoC phase, however, with only 5 electrons per atom is near the limit of hP2 stability. It is reasonable that a small percentage of Fe, Ni, Co or interstitial nitrogen stabilizes MoC by simply increasing its electronic concentrations.

V. REFERENCES

1. H. Moissan, Compt. Rend **116**, 1225 (1893); **120**, 1320-26 (1895); **125**, 839-44 (1897); **138**, 1558 (1904).
2. H. Kuo, G. Hägg, Nature **191**, 245-256 (1952).
3. D. H. Killeffer and A. Linz, **Molybdenum Compounds**, Interscience, New York, 1952.
4. **Metals Handbook**, 8th ed., Vol. 8, p. 279, American Society of Metals, 1972.
5. E. Rudy, "Compendium of Phase Diagram Data", Air Force Materials Laboratory, Wright-Patterson AFB, Ohio, AFML-TR-65-2, Part V (June 1969).

6. E. Rudy, S. Windisch and Y. A. Chang, Air Force Materials Laboratory, Wright-Patterson AFB, Ohio, AFML-TR-65-2, Part I, Vol. I (March 1965).

7. E. Rudy, S. Windisch and J. R Hoffman, Air Force Materials Laboratory, Wright-Patterson AFB, Ohio, AFML-TR-65-2, Part I, Vol. VI (Jan. 1966).

8. E. Rudy, S. Windisch A. J. Stosick and J. R. Hoffman, Air Force Materials Laboratory, Wright-Patterson AFB, Ohio, AFML-TR-65-2, Part I, Vol. XI (April 1967); Trans. Metall. Soc. AIME **239**, 1247-67 (1967).

9. E. Parthe, V. Sadagoran, Acta Cryst. **16**, 202-205 (1963).

10. F. A. Shunk, **Constitution of Binary Alloys**, 2nd Supplement, McGraw-Hill, New York, 1969.

11. R. Hultgren, P. D. Desai, D. T. Hawkins, M. Gleiser and K. K. Kelly, **Selected Values of the Thermodynamic Properties of Binary Alloys**, Am. Soc. for Metals, Metals Park, Ohio, 1973.

12. L. E. Toth, **Transition Metal Carbides and Nitrides**, Academic Press, New York and London, 1971, pp. 79-84.

13. J. Schuster, E. Rudy, H. Nowotny, Monatsh. Chem. **107**, 1167-76 (1976).

14. E. Rudy, B. F. Keifer and E. Baroch, Plansee. für Pulvermetal. **26**, 105-16 (1978).

15. L. Brewer and R.H. Lamoreaux, "Molybdenum: Physicochemical Properties of Its Compounds and Alloys, Part II, Phase Diagrams", pp. 222-25, Atomic Energy Review Special Issue No. 7, International Atomic Energy Agency, Vienna, 1980.

16. L. Brewer, D. G. Davis, Metall. Trans. **15A**, 67-72 (1984).

17. R. Stimach, Chemistry 196 report, Univ. California, Berkeley, 1983.

18. H. Nowotny, E. Parthe, B. F. Kieffer, F. Benesovsky, Monatsh. Chem. **85**, 255 (1954).

19. E. Rudy, Air Force Materials Laboratory, Wright-Patterson AFB, Ohio, AFML-TR-65-2, Part V, (1969).

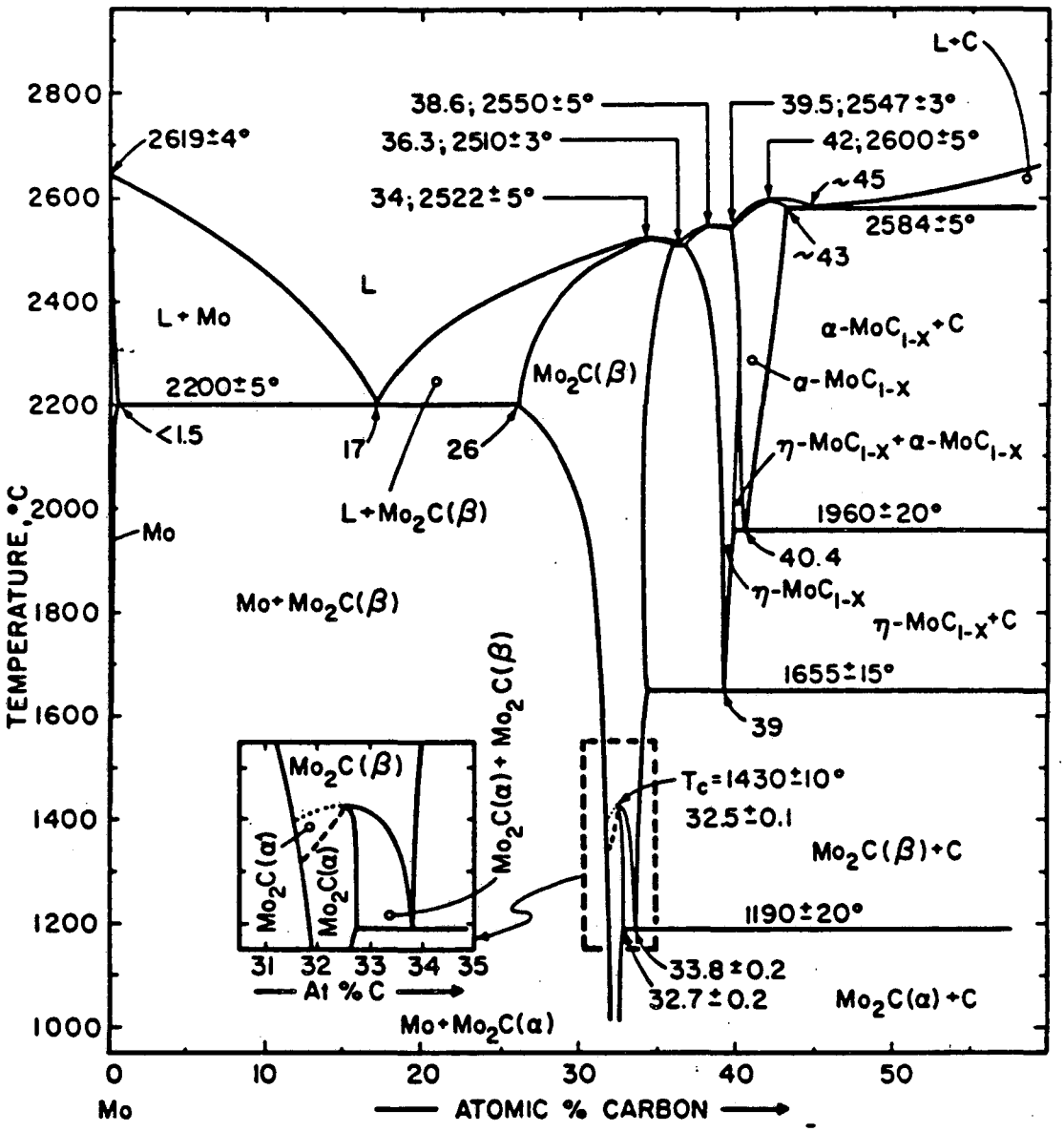

FIG. 1. The molybdenum carbon phase diagram determined by Rudy, et al.[19]

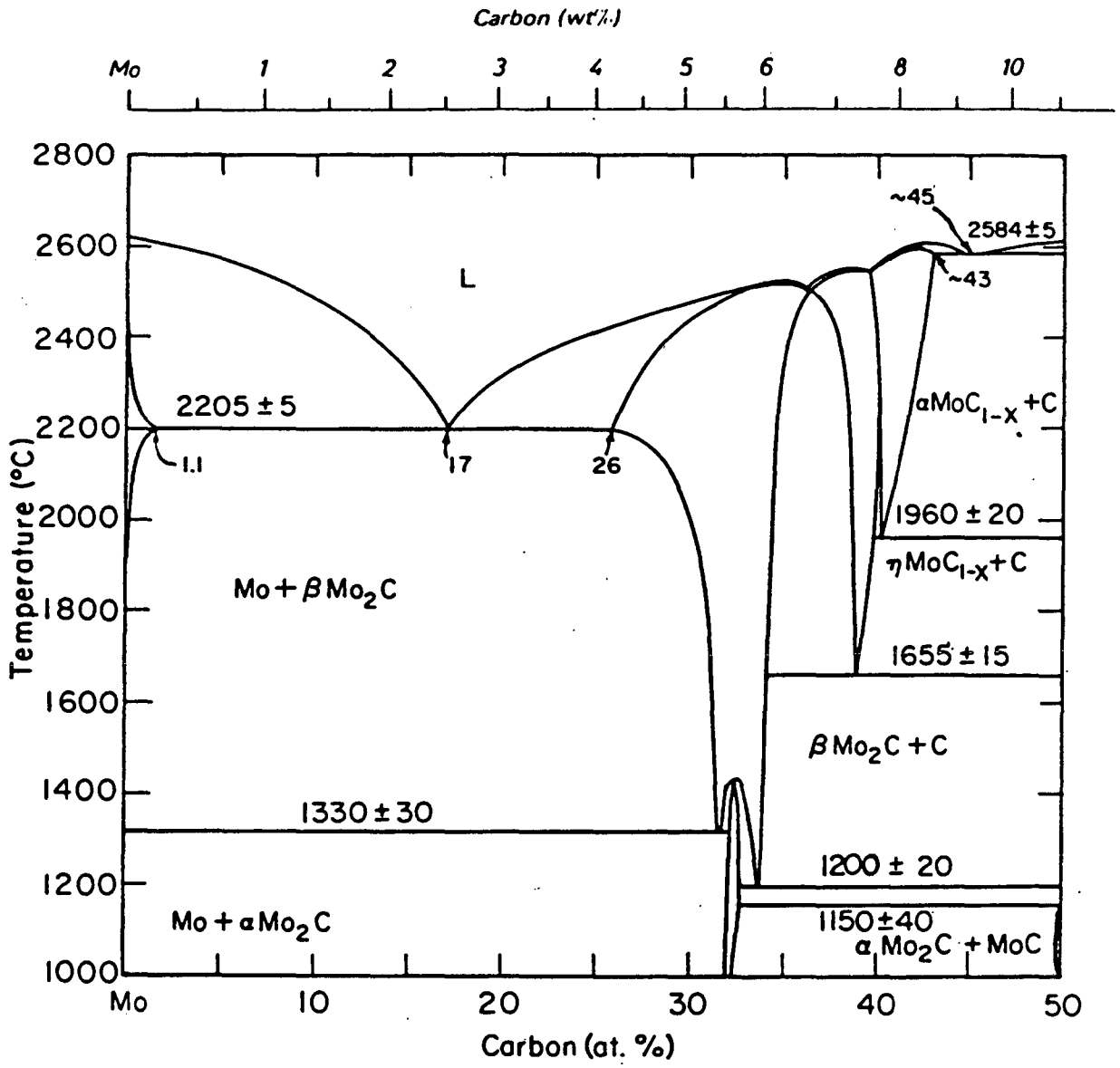

FIG. 2. The molydenum-carbon phase diagram as reported by Brewer and Lamoreaux.[15] MoC is included as a stable phase below 1150 ±40 °C.

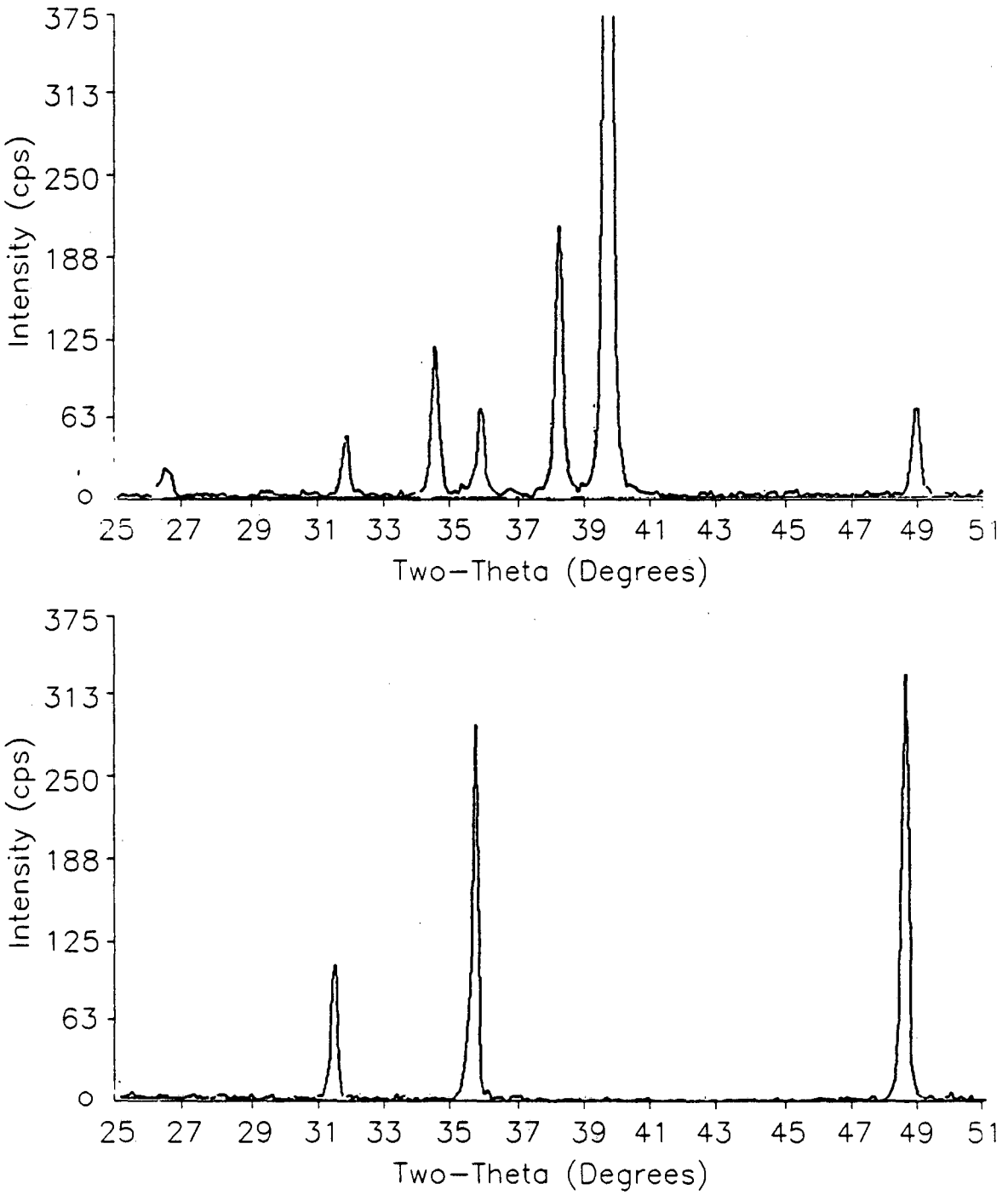

FIG. 3. X-ray diffraction pattern of a sample containing MoC, Mo_2C and traces of carbon. The lower pattern is that of pure WC. The MoC and WC reflections are compared.

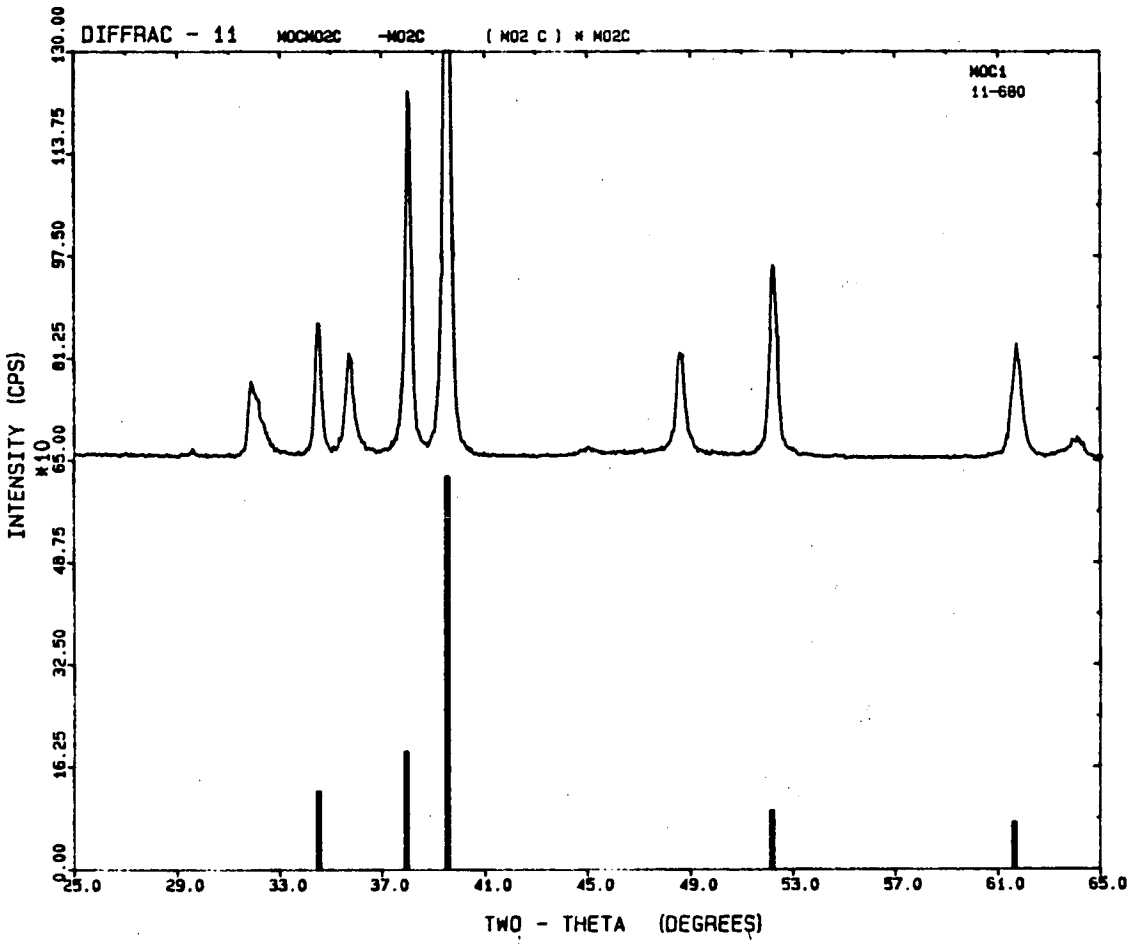

FIG. 3a. The x-ray diffraction pattern of a sample containing Mo_2C and γ-MoC. The pattern below is the one reported in the JCPDS file for the Mo_2C phase.

FIG. 3b. The optical micrograph of a sample containing Mo_2C, γ-MoC and C at 160× using unpolarized light. The crystallites of Mo_2C and γ-MoC are the white areas and dark grey areas, respectively. The dark material is carbon and the black areas are voids.

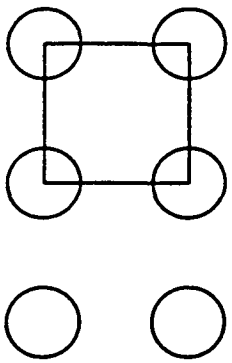

A A stacking of Mo
atoms in WC type structure
a=2.898 Å c=2.869Å

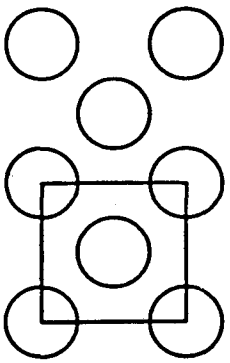

AB,AB hexagonal close-packed
Mo atoms
a=3.002Å c=4.724Å

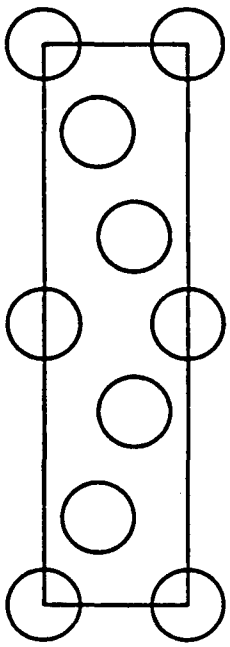

ABCACB,ABCACB
stacking in the
hMoC1-x phase
a=3.006Å
c=14.610Å

FIG. 4. Unit cell parameters of MoC, Mo_2C and η-MoC_{1-x}.

TABLE 1. Gradient furnace experiment temperatures and corresponding phases found.

T (°C)	Phases
800	Mo_3C_2, Mo_2C + C
900	MoC, Mo_2C, C
950	MoC, Mo_2C, C
970	MoC, Mo_2C, C
1030	MoC, Mo_2C + C
1075	traces MoC, Mo_2C + C
1120	Mo_2C + C

TABLE 2. X-ray data for γ-MoC in equilibrium. Graphite was used as an internal standard.

Int.	d calc.	hkl
MS	2.8115	001
S	2.5078	100
VS	1.8724	101
M	1.4515	110
W	1.4080	002
M	1.2984	111
ST	1.2557	200
M	1.2280	102
M	1.1470	201

TABLE 3. X-ray data of Mo_2C in equilibrium. Graphite was used as an internal standard.

Int.	d calc.	hkl
M	2.6047	100
ST	2.3624	002
VST	2.2794	101
M	1.7506	102
MST	1.5036	110
MW	1.3486	103
W	1.3042	200
M	1.2696	112
M	1.2550	201
W	1.1839	004

TABLE 4. Binary and ternary compounds of hP2 symmetry with a 5-6 electron per atom range.

MoC	MoN	RuC
WC	WN	OsC
TaN	MoP	IrB
$Nb_{10}N_9$	ReC	
ReB	RuB	
	OsB	

$MoC_{1-x}N_x$

$WC_{1-x}N_x$

PART 2. SECTION 1: ENGEL-BREWER THEORY

I. INTRODUCTION

Most of the elements in the periodic table are metals. Various combinations of metals can produce an astronomical number of alloys. The bonding involved in alloys is not understood as well as the bonding of nonmetallic compounds. Rigorous quantum mechanical calculations cannot realistically describe the properties of intermetallics. However, regular solution theories have been applied reasonably well to systems that do not exhibit strong interactions among their constituent elements. There is, however, another class of alloys of extraordinary stability and strength that simple solution theories cannot describe. These unusual intermetallic compounds are stabilized by an acid-base-type interaction which can be explained in terms of the Engel-Brewer theory.[1-2]

The Engel-Brewer theory is a valence bond approach to bonding in transition metals. It is widely used to explain bonding structures and thermodynamic stability in metallic systems. This study is focused to further characterize the acid-base effect in the context of Engel-Brewer theory. Thermodynamic data have been obtained that could be used to develop simple bonding models. These models would provide reliable predictions for this astronomical number of compounds that could not realistically be studied in the laboratory.

II. VALENCE BOND THEORY

A basic understanding of the valence bond theory is essential to understand the Engel-Brewer model. In the valence bond theory,[3-4] atoms

of nonmetals interact to form molecules which are held together by electron pair bonds. These electron pairs occupy bonding orbitals which are formed by overlap of atomic orbitals from adjacent atoms. Chlorine atoms with the valence electronic configurations $3s^2 3p^5$ forms chlorine molecules with one electron pair bond per atom by overlap of the orbitals containing the unpaired electrons. Phosphorus in its ground state $3s^2 3p^3$ has 3 unpaired p-electrons. It uses these electrons to form three bonds per atom in the puckered graphite-like structure of black phosphorous or in the tetrahedral P_4 molecule that is found in the gas phase and in solid white phosphorus. Silicon with its promoted sp^3 configuration can form four electron pair bonds in the diamond structure.

The valence model can also be applied to metals.[5] Metals can also form electron-pair bonds except that these bonds are distributed among the neighboring atoms in the lattice and the electrons become somewhat delocalized. Sodium can form an electron pair bond with its single 3s electron. This bond, however, is distributed to eight nearest neighbors and to even more distant neighbors of the body-centered cubic (bcc) structure. Magnesium, on the other hand, with $3s^2$ configuration cannot form electron-pair bonds. The low energy 3sp excited state with two unpaired electrons form two electron pair bonds that are distributed among the 12 nearest neighbors of the Mg hexagonal close-packed (hcp) lattice. Similarly aluminum uses the $3sp^2$ promoted state to form three electron pair bonds per atom in the face-centered cubic (fcc) lattice. The promotion energy required to obtain these excited states in the gaseous atoms is compensated by the energy from the additional bonding in the solid state. In all three examples described there is a correspondence between the electronic configuration and the crystal

structure. The s^1 configuration corresponds to the bcc structure, the s^1p^1 configuration to hcp, the sp^2 to ccp, and the sp^3 corresponds to the diamond (tetrahedral bonding) structure. The stability of the elements, as indicated by the increase in the atomization energy from Na to Al, increases as the number of bonds per atom increases. The application of the valence bond theory for both metals and nonmetals can be used to explain crystal structure correlations and bonding strengths.

Hume-Rothery[6] was the first to recognize that crystal structure can be correlated with the valence-electron count. He pointed out that intermetallic compounds with the same average number of valence electrons had the same crystal structure. His rules could not be applied to the transition metals because counting the d-electrons in the total number of valence electrons did not yield reliable predictions. The Engel-Brewer theory[1,7-9] uses only the sp-electrons to correlate structure with electron concentration. The d electrons, however, indirectly influence the crystal structure by fixing the sp electron concentration. The d-orbitals which belong to the inner-shell are much more localized and cannot bond effectively with the sp orbitals. They can be used to prepare the best bonding electronic configuration. This will be a promoted state with the maximum number of unpaired electron. This configuration becomes important for bonding only if its promotion energy is paid off by the bonding enthalpy obtained in going from the gas to the solid. The s and p orbitals are shielded less by the closed shells and extend far out into the metal, determining long-range structure.

Engel[7-9] first assigned an electron configuration to the three major crystal structures of transition metals. If n is the total number

of valence electrons, the $d^{n-1}s$ electronic configuration corresponds to the bcc structure, the $d^{n-2}sp$ to the hcp, and the $d^{n-3}sp^2$ to the fcc structure. This electron concentration-crystal structure correlation can be applied to binary alloys.[10] The bcc structure is observed when the number of sp electrons is less or equal to 1.5. The hcp structure is observed when the number of sp electrons is in the range of 1.7 to 2.1. The fcc structure is correlated with an electronic range of 2.5 to 3.2.

Brewer[1] quantitatively confirmed the Engel correlations by using spectroscopic data for the gaseous atoms. The ground state and the promotion energies to the excited states for most transition elements are known.[12] By comparing promotion energies and bonding enthalpies for states with the same number of valence electrons, Brewer showed which configurations are most important for bonding in the solid. The structure of elemental Mo is chosen as an example. The lowest configurations of the gaseous atom are d^3s^2, d^5s, and d^4sp. The d^4s^2 configuration has only four bonding electrons. The d^5s^1 and d^4sp, with 6 bonding electrons, will bond much more strongly in the solid. The d^5s, which is lower in energy than d^4sp by 80 kcal, is expected to predominate in the solid. This configuration corresponds to the bcc structure. Mo is found to have only the bcc structure at all temperatures and pressures, as predicted by the Engel-Brewer correlations. In Fig. 1.1 the energies for the electronic configurations are shown as bands. This is because there are several spectroscopic states for each configuration corresponding to different combinations of spin and orbital momenta of the electrons. The energy of each configuration is often taken as the average of the energies of the states of configuration. Brewer[11] has

shown that using the energy of the lowest state of configuration to determine its bonding energy is equally as accurate as using the average over all states.

The Engel-Brewer theory quantitatively describes the bonding contribution of the s,p and d electrons. From spectroscopic data, the energies of the d^{n-1} and d^{n-2} electronic configurations of the gaseous atom are known. The enthalpies of sublimation which correspond to the ground state of the gaseous atoms are also known. Combinations of heats of sublimation with promotion energies to d^{n-1} (bcc configuration) of $d^{n-2}sp$ (hcp configuration) yield the bonding enthalpy of the valence state. The bonding enthalpy of the 5s and 5p electrons has been estimated from the experimental bonding enthalpies of strontium and cadmium. The bonding enthalpies of the 4d electrons are found by simply subtracting the s and p contribution from the total bonding enthalpy of the valence state.

The bonding enthalpy per d electron for the 4d electrons is illustrated in Fig. 1.2 As the number of unpaired d electrons increases, the bonding energy per electron decreases, partly because of increasing bond order and partly because of crystal field effects. As the bond order rises the repulsion between electron-pair bonds becomes more severe and bonding strength drops. In a non-spherically symmetric field, the d orbitals split so that some are more extended and some are more contracted than their average. The first unpaired bonding electron occupies the most extended d-orbitals to achieve maximum overlap. As the number of electron increases to five, the most contracted and worst bonding orbitals are occupied and the energy per bonding electrons falls sharply. When the number of electrons exceeds five, nonbonding pairs

begin to form. These occupy the most contracted orbitals, leaving the most extended orbitals to be used for bonding. The bonding per electron rises again as unpaired electrons decrease from five to one.

This quantitative estimate of d-electron bond strength can be used to predict thermodynamic properties for the hcp and bcc structures even if they are not observed. The internally paired electrons that do not contribute to the bonding strength of the pure metal can contribute to the bonding strength of intermetallic compounds. Nonbonding pairs of one metal are donated to vacant orbitals of another metal, resulting in externally stable acid-base compounds. The basicity of each of the electron pairs will depend on the magnitude of the crystal field splitting that the d orbitals undergo.

The Engel-Brewer principles that have been applied to explain structure and stability of pure metals can be used to characterize this unusual class of alloys stabilized by a generalized acid-base interaction.

III. ACID-BASE REACTIONS IN METALS

A. Generalized Lewis Acid-Base Interactions Between Metals

Brewer has demonstrated that combination of d-electron deficient metals, such as Ti, Zr, Hf, V, Nb and Ta, with the d-electron rich platinum group metals form alloys with high heats of formation. When platinum metal interacts at 1000 °C with zirconium carbide, a very stable intermetallic $ZrPt_3$ is formed

$$ZrC + 3Pt \longrightarrow ZrPt_3 + C$$

Carbon is displaced from the carbide by platinum. This is a remarkable result because carbides are considered only second to oxides and

fluorides in stability. Platinum and its relatives are generally accepted as inert. These metal-metal reactions are considered analogous to the Lewis acid-base reactions that are common among nonmetals.

A Lewis base is a substance that can provide an electron pair to form a bond. A Lewis acid is a substance with a vacant orbital that can accept an electron pair donated by the acid. The BF_3-NH_3 adduct is a classic acid-base material. The nonbonding pair on NH_3 is transferred to the empty p_z orbital of the boron

$$BF_3 + NH_3 \longrightarrow F_3B : NH_3$$

Gallium arsenide can also be considered as Lewis acid-base stabilized compound. The arsenic (s^2p^3) has a nonbonding electron pair which can be donated to the empty p-orbital of gallium (sp^2) so that each achieves the sp^3 electron configuration necessary for the diamond structure.[13] In GaAs the more electronegative arsenic transfers electrons to the more electropositive gallium. However, once the gallium-arsenic bond is formed, the electron density is shifted toward the arsenic to reduce the negative charge on the gallium.

The acid-base reaction in Brewer's alloys occurs because nonbonding electron pairs on the base metal combine with the vacant d orbitals of the acid metal. This is clearly illustrated in the reaction of palladium with vanadium to form an alloy of approximate composition Pd_3V_2. Palladium has a $d^{10}s$ ground state electron configuration for the gaseous atom. The promotion energy required to attain the d^7sp^2 configuration required for its fcc structure in the metal is offset by the increase in the number of bonding electrons from 0 to 6. In addition to the 6 bonding electrons, the metal has 2 nonbonding electron pairs that can be

used for acid-base bonding. Vanadium has a d^3s^2 ground state configuration. Transfer of an s electron to the d orbital yields the d^4s bonding configuration which corresponds to the bcc structure. Vanadium metal has a total of 5 bonding electrons and a vacant d orbital, in addition to the vacant p orbitals that can accept electron pairs to form acid-base bonds. The crystal structure of the V_2Pd_3 alloy is face-centered cubic, indicating an average sp electron concentration of 3 sp electrons per atom. Since a total of 40 electrons is contributed by both atoms (2 mol V × 5 e + 3 mol Pd × 10 e = 40 e) and 15 (5 atom × 3s,p e^- = 15 e^-) have to occupy the s and p orbitals, the remaining 25 will occupy the d orbitals. The occupancy in terms of electrons per atom is 3 for the sp orbitals and 5 for the d orbitals in the alloy. The total number of bonding electrons has increased from an average of 5.5 per atom for the pure metals to 8 per atom for the intermetallic (Fig. 1.3). The increase in the bonding strength of the alloy is due to the transfer of internally paired electrons from the palladium to the vanadium.

The bonds formed from this type of sharing of electron pairs are not as strong as bonds formed by equal electronic contributions at the interacting atoms. Brewer has shown this by calculating enthalpies of formation for acid-base stabilized alloys using the bonding enthalpies found for d electrons for the pure metals. With the acid-base phases, the experimental enthalpy values are significantly smaller than the calculated values, even though these are still unusually large for intermetallics. The large charge transfer from the base metal to the acid metal will increase the formal charge of the acid metal drastically. This high formal charge must be reduced by departure of bonding electrons <u>via</u> a back-bonding type of mechanism.

This acid-base reaction is much more complicated than sharing of electron pairs among atoms. Many factors need to be considered to accurately characterize this novel bonding and develop models that will allow prediction of thermodynamic properties and phase diagrams of the transition elements. This will require quantitative measurements of the acidities and basicities of combinations of transition metals with the same quantum shells as well as with different quantum shells and the measurement of the bonding contributions of the various donating pairs of a base to the various accepting orbitals of an acid.

Many typical Lewis acids and bases can be titrated against one another. Titrations provide a way of monitoring acid-base reactions as a function of concentration. Transition metals are essentially poly-functional acids and bases. To measure quantitatively the transition metal acid-base strengths, titrations of the acid by the base and measurements of the activity coefficient or the partial-excess-molar Gibbs free energy as a function of concentrations are needed. This study concentrates on performing this type of titration. Although it appears that the concept is very similar to the titrations of traditional acids and bases, the experimental approach unfortunately does not employ beakers, burets and indicators. These titrations are performed by equilibrations of pairs of oxides of the acid with the base metal and measurements of the acid concentration and by high temperature solid state galvanic cell measurements.

B. Previous Work

The acidity and basicity of transition metals has been qualitatively studied and trends of acid-base strength have been established. Wengert, in his study of various intermetallics of zirconium with elec-

tron-rich metal of the right side of the periodic table,[14] has shown that the platinum group metals are the best bases. His plot of the partial molar Gibbs free energy of Zr versus atom number of base metal shows that the maximum base strength occurs between iridium and platinum (Fig. 1.4). Gibson[15] determined thermodynamic activities of a variety of group IVB-VIB elements with the platinum group metals. He obtained limits for the Gibbs free energy of formation of intermetallic compounds and concluded that crystal field effects reduce the bonding ability of certain valence d orbitals. Choudary, Gingerich and Cornwell[16] have measured Gibbs free energies of formation of Ti-Ir phases and Ti-Pd phases by mass spectrometry. Meschter and Worrell[17] also measured Gibbs free energies at 1300 K of titanium-platinum alloys by solid-state galvanic cell measurements. Cima[19] compared the base behavior of Pd and Rh using galvanic cell measurements. He found that at low concentrations of niobium, palladium is a very effective base. As indicated by measurements of niobium activity coefficient in rhodium by Kleykamp,[20] rhodium is a less effective base than palladium at low niobium concentration. But at higher concentrations of Nb, Rh becomes a better base than palladium.

C. Applications

In reducing atmospheres, ZrO_2 and Pt react. This explains erroneous temperature readings in Pt/Pt-Rh thermocouples contained by ZrO_2.[21] In the presence of Pt, actinide metals can be obtained from their oxide. The Pt actinide alloy is initially formed. The actinide is then isolated from the alloy by vaporization[22]

$$AmO_2 + 2H_2 + 5Pt \longrightarrow AmPt_5 + 2H_2O$$

$$AmPt_5 \longrightarrow 5Pt + Am(g)$$

At elevated temperatures, platinum group metal catalysts are reported to interact with their TiO_2 supports.[23] These catalysts at low temperature (200 °C) exhibit the ability to adsorb hydrogen or carbon monoxide. At 500 °C, however, the adsorption of CO and H_2 disappears. The noble metal has reacted with the oxide support to form intermetallic compounds

$$TiO_2 + 2H_2 + 3Pt \longrightarrow TiPt_3 + 2H_2O.$$

VI. REFERENCES

1. L. Brewer, Science **161**, 115 (1968).
2. L. Brewer, Lawrence Berkeley Laboratory Report, LBL-3720, rev., May 1977.
3. W. L. Jolly, **Modern Inorganic Chemistry**, McGraw-Hill, New York, 1984.
4. C. E. Mortimer, **Chemistry: A Conceptual Approach**, 4th ed., Van Nostrand, New York, 1979.
5. L. Brewer, J. Mat. Educ. **6**, 773 (1984).
6. W. Hume-Rothery, **The Metallic State**, Oxford Univ. Press, Oxford, 1931; W. Hume-Rothery, **Structures of Metals and Alloys**, Institutes of Metals, London, 1936.
7. N. Engel, Ingenioeren **M101** (1939); N. Engel, Ingenioeren **M1** (1940).
8. N. Engel, Powd. Met. Bull. **7**, 8 (1954).
9. N. Engel, Acta Met. **15**, 557 (1967).
10. L. Brewer, Acta Met. **15**, 553 (1967).

11. L. Brewer, in **Phase Stability in Metals and Alloys**, P. Rudman, J. Stringer, R. L. Jaffee, Eds., pp. 39-61, 241-43, 246-49, 344-46, 560-68, McGraw-Hill, New York, 1967.

12. C. E. Moore, "Atomic Energy Levels", U.S. Gov't Print. Off., Washington, D.C., Vol. I (1949), Vol. II (1952), Vol. III (1958).

13. L. Pauling, Proc. Roy. Soc. London Ser. A **196**, 343 (1949); L. Pauling, **The Nature of Chemical Bond**, 3rd ed., Cornell Univ. Press, Ithaca, 1960.

14. L. Brewer and P. Wengert, Metall. Trans. **4**, 83 (1973).

15. J. Gibson, et al., Metall. Trans. **15A**, 2075 (1984).

16. U. V. Choudary, K. A. Gingerich and L. R. Cornwell, J. Less-Common Metals **50**, 201 (1976).

17. U. V. Choudary, K. A. Gingerich and L. R. Cornwell, Met. Trans. **8A**, 1487 (1977).

18. P. S. Meschter and W. L. Worrell, Metall. Trans. **7A**, 299 (1976).

19. M. J. Cima, Ph.D. dissertation, Univ. of California, Berkeley, 1985, LBL-21951

20. H. Kleykamp, J. Less-Common Metals **83**, 105 (1982).

21. W. J. Weppner, J. Electron. Chem. **84**, 339 (1977).

22. E. Raub and G. Falkenburg, Mettalwiss. Tech. **27**, 669 (1973).

23. S. J. Tanster, S. C. Fung and R. L. Gowten, J. Am. Chem. Soc. **100**, 170 (1978).

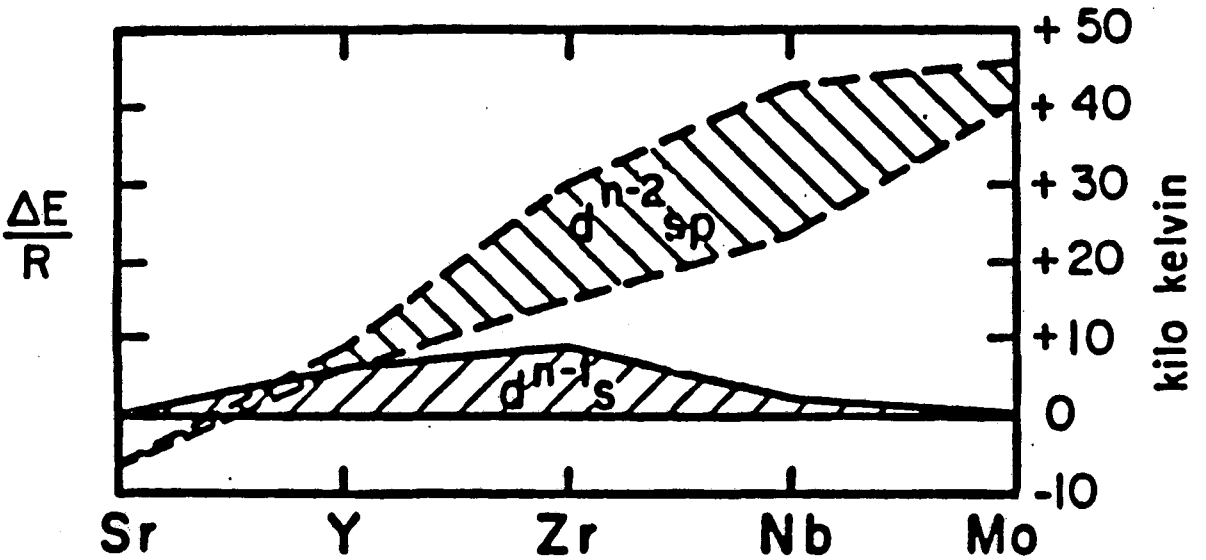

FIG. 1.1. The relative energies of the $d^{n-1}s$ and the $d^{n-2}sp$ configurations for the gaseous atoms of the second row transition metals. The energies of those electronic configurations are shown as bands. This figure was provided by L. Brewer.[1]

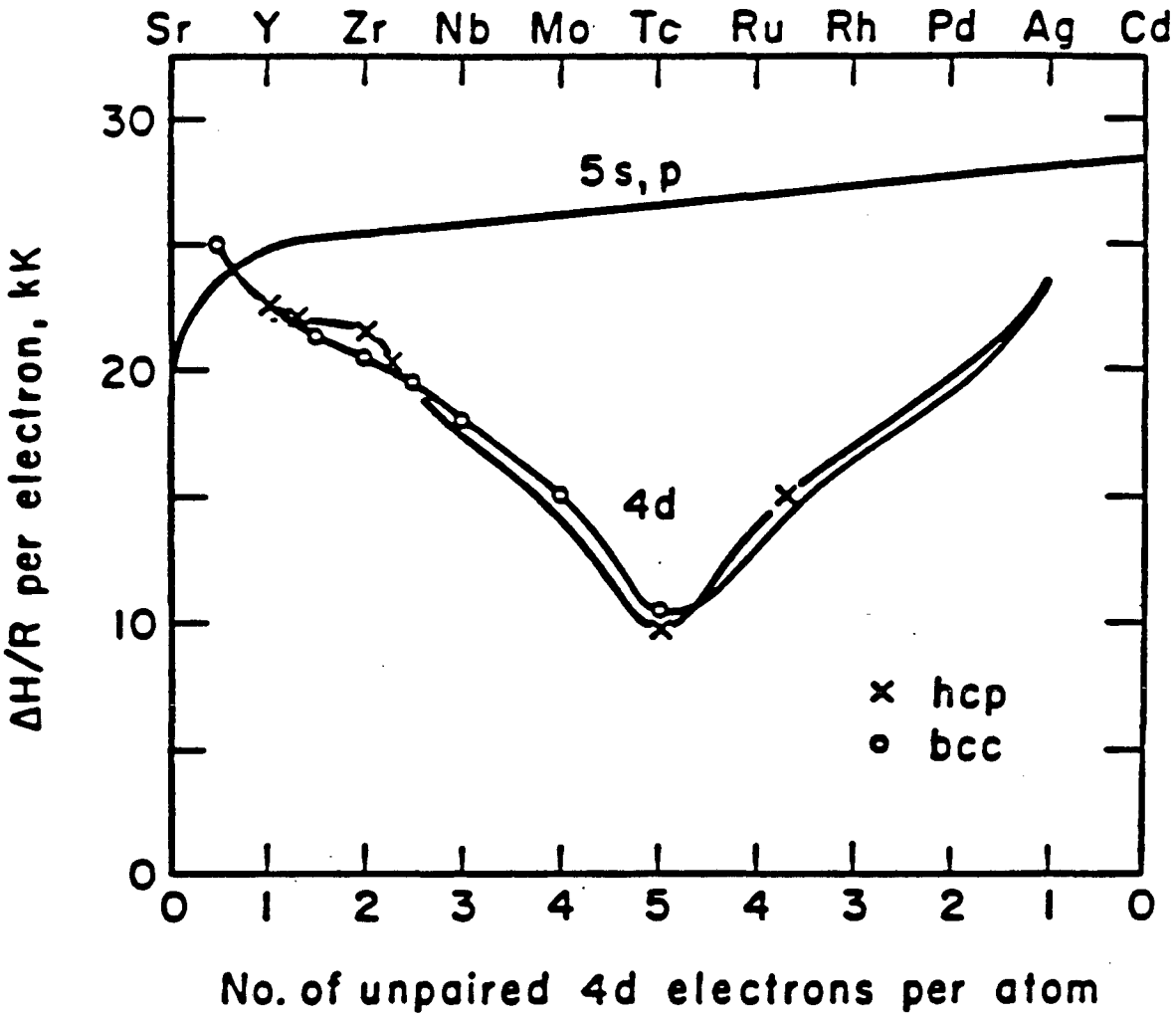

FIG. 1.2. The valence state bonding energy per unpaired electron in kilo-Kelvin per gram atom for the second-row transition metals is illustrated in this figure. The top curve presents the bonding enthalpy of a s,p electron for the metals of this row. The bottom curve presents the bonding enthalpy of a 4d electron as a function of bond order (number of unpaired d electrons in valence state). This diagram was provided by L. Brewer.[1]

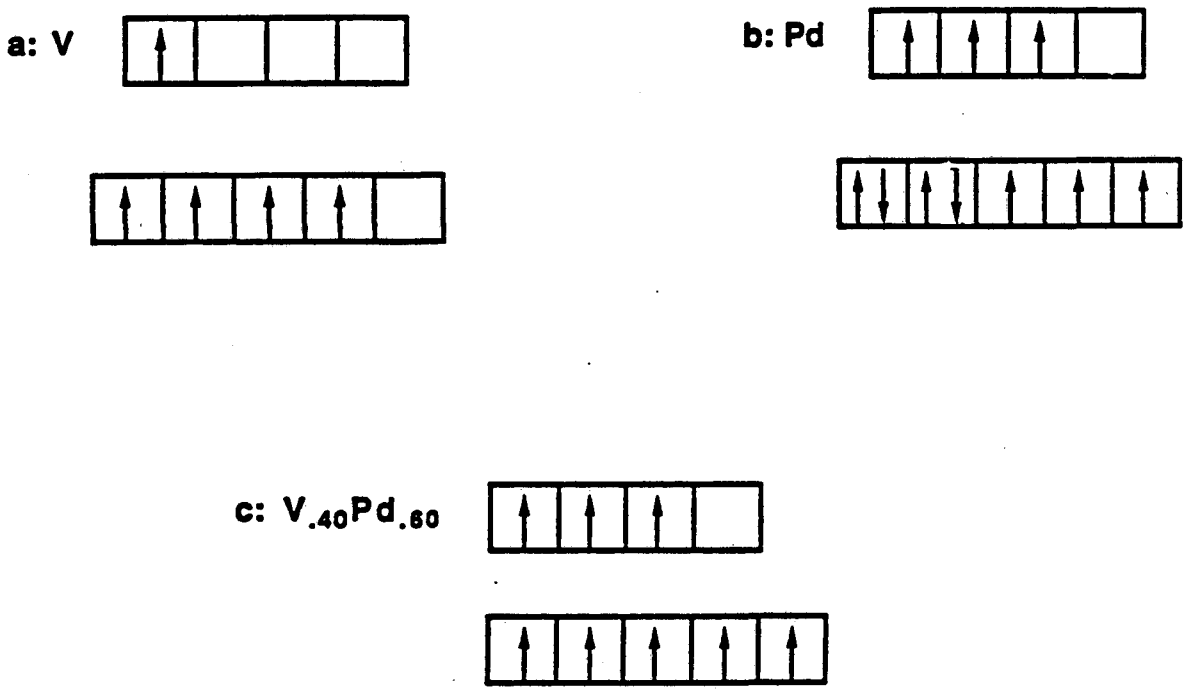

FIG. 1.3. The valence state electron configuration for one atom of vanadium, palladium and of the $V_{0.40}Pd_{0.60}$ alloy are illustrated in this figure. In each of the a, b and c representations the first row of boxes corresponds to the 6s and 6p orbitals. the second row represents the 5d orbitals. The number of bonding electrons has increased from 5.6 per atom for the separate elements to 8 electrons per atom in the alloy.

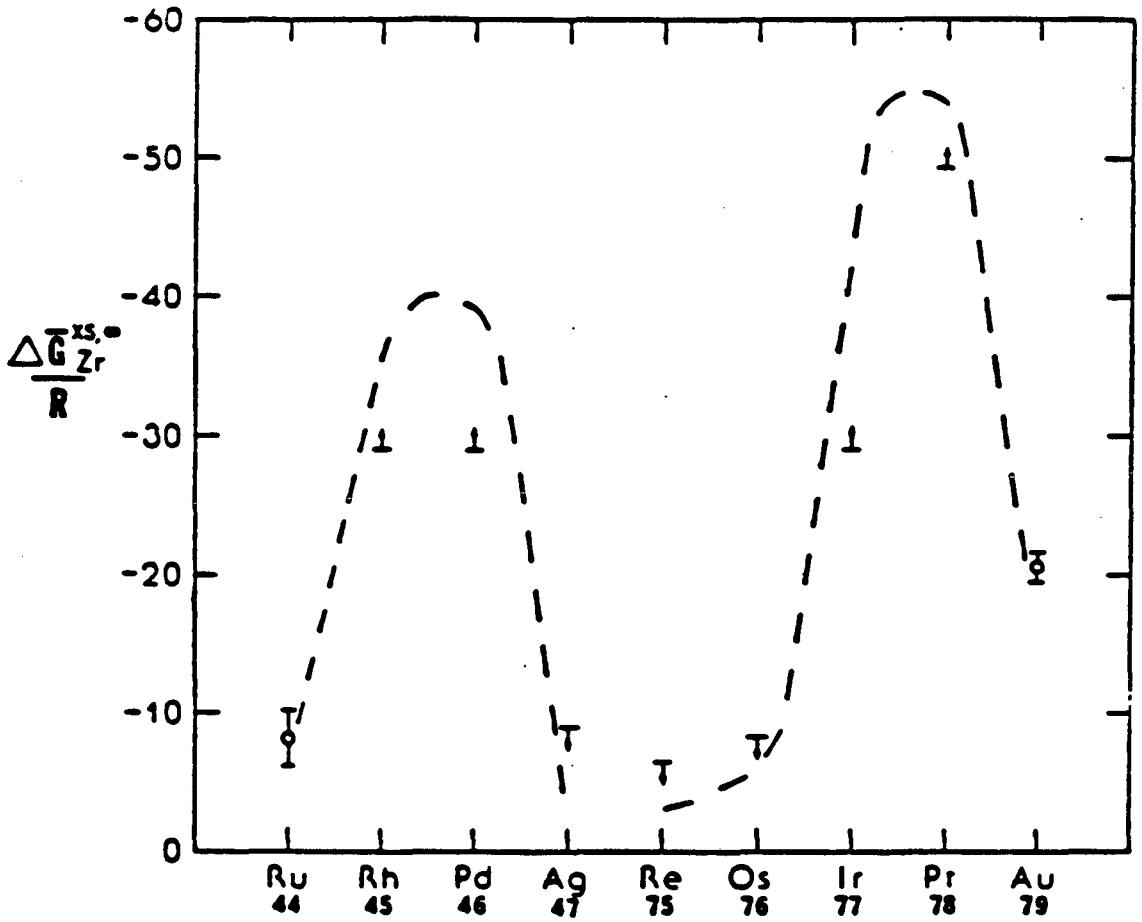

FIG. 1.4. Partial molar Gibbs free energy in kilo-Kelvin per gram atom of Zr (at infinite dilutions at 1800 K) versus the atomic number of the base metals. This diagram was obtained from L. Brewer.[14]

PART 2. SECTION 2: THEORY AND EXPERIMENTAL PROCEDURES

I. THEORY

A. Oxide Equilibria

Vanadium, titanium and niobium have a large number of oxides with well-characterized structures and thermochemical quantities. Vanadium, for example, in addition to the common VO, V_2O_3, VO_2 and V_2O_5 phases, has several suboxides and the nonstoichiometric Magnelli phases. Equilibration of any adjoining pair of these oxides fixes the activity for both the oxygen and the vanadium. A vanadium-palladium alloy in equilibrium with a pair of oxides has the same vanadium activity as the vanadium activity in the oxides. The activity of any component is equal in all three equilibrium phases.

$$a_V^{\text{oxides}} = a_V^{\text{alloy}}$$

The VO, V_2O_3 and V_{Pd} ternary region at 1000 °C and ordinary pressures is shown in Fig. 2.1. Any composition of the three components (O, Pd, and V) in this region, according to the phase rule, will yield the two oxides and the alloy in equilibrium. The equilbrium reaction for the three phases can be written as

$$3VO + (Pd) \xrightarrow{1000^{\circ}C} V_2O_3 + V_{(Pd)} \qquad (1)$$

In this reaction a small amount of palladium, in contact with VO, withdraws vanadium from the oxide to produce V_2O_3 and the alloy. The Gibbs free energy of the reaction can be expressed in terms of the partial molar Gibbs free energy of vanadium.

$$\Delta G^{o} = \Delta G^{o}_{f}V_2O_3 - 3\Delta G^{o}_{f}VO$$

$$0 = \Delta\bar{G}V + \Delta G^{o} \text{ at equilibrium}$$

$$0 = \Delta G_V - 3\Delta G^{o}_{f}VO + \Delta G^{o}_{f}V_2O_3$$

It can also be written in terms of the activity of vanadium on the alloy.

$$\Delta\bar{G} = RT \ln a_V = -\Delta G^{o}$$

$$a_V = \exp(-\Delta G^{o}/RT)$$

To calculate $-\Delta G/RT$, the values of the Gibbs energy functions $-(G^{o}-H^{o}_{298}/RT)$ for the vanadium and the oxides are combined to yield the difference in the Gibbs energy function $-(\Delta G^{o}-\Delta H^{o}_{298}/RT)$ for Eq. 1. The $\Delta H^{o}_{298}/RT$ values are then combined to obtain $\Delta G^{o}/RT$. The literature values of $-(G^{o}-H^{o}_{298}/RT)$ and $\Delta H^{o}_{298}/RT$ for vanadium oxides are listed in Table 2.1. They were obtained from the recent compilation of vanadium oxide thermodynamics by Brewer and Ebbinghaus.[1]

The analysis of the alloy to obtain the concentration of vanadium yields the excess partial molar Gibbs free energy or the activity coefficient (γ).

$$a_V = x_V\gamma_V$$

$$\gamma_V = \frac{a_V}{x_V}$$

By changing the oxide pair, the concentration of vanadium in the alloy phase and the vanadium activity will change. Therefore, for a

large number of oxide pairs the activity coefficient of vanadium in a range of compositions can be obtained and consequently the beginning of a titration curve of activity coefficient versus concentration can be constructed. The oxide-alloy equilibration experiments result in the derivation of the three-component phase diagram at fixed temperature and pressure. Knowledge of the complete ternary diagram is essential for sample preparation for galvanic cell experiments described below.

The measurement of oxide equilibria is a very reliable technique for obtaining thermochemical data. It has few systematic errors. It is not, however, sufficient to provide a complete set of data required to construct the metal acid-base titration curve. The activity of the metal oxides dictates the composition of the intermetallic-phase in equilibrium with the oxides. In the vanadium-palladium system the large activity drop across the V_2O_3 phase limits the concentration of vanadium in the alloy that is in equilibrium with V_2O_3-V_3O_5 to a very small amount. The activities of vanadium in intermediate alloy compositions have to be determined by a different technique.

B. High Temperature Solid Electrolyte Cells

High temperature solid electrolyte cells are used to compliment the oxide equilibration method. The alloy composition needed to fill the gaps in the titration curve will be in equilibrium with a single oxide phase. In these systems the partial pressure of oxygen in equilibrium with an oxide alloy combination fixes the activity of each element. The partial pressure of oxygen is related to the vanadium activity by the equation

$$\Delta G_f V_2O_3 = 2\Delta\bar{G}_V + \frac{3}{2}RT \ln PO_2 \qquad (2)$$

The partial pressure of oxygen can be measured with solid state electrochemical cells for measurements of thermodynamic properties of ceramic and metallic phases. These cells are essentially concentration cells that correlate the oxygen partial pressure differences between two electrodes to EMF. The cell used in this study is of the following form

$$\text{Pt} \mid \text{Ta, } \text{Ta}_2\text{O}_5 \mid \underset{\text{electrolyte}}{\text{Y}_2\text{O}_3\text{-ThO}_2} \mid \underset{\text{cathode}}{\text{V}_{(\text{Pd})}\text{V}_2\text{O}_3} \mid \text{Pt}$$

anode

The anode or reference electrode consists of a mixture of tantalum and tantalum pentoxide. The half-reaction occurring at this electrode is

$$2\text{Ta} + 5\text{O}^{-2} + 10\text{e}^- \longrightarrow \text{Ta}_2\text{O}_5 \qquad (3)$$

The electrolyte is a sintered solid solution of yittria and thoria which conducts oxygen anions at elevated temperature ($T > 800$ °C). The cathode or working electrode is a combination of V_2O_3 and the palladium-vanadium alloy. The half-reaction at this electrode is

$$6\text{e}^- + \text{V}_2\text{O}_3 \longrightarrow 2\text{V} + 3\text{O}^{2-} \qquad (4)$$

The overall balanced cell reaction is

$$0.6\text{Ta} + \text{VO}_{3/2} \longrightarrow 0.3\text{Ta}_2\text{O}_5 + \text{V}_{(\text{Pd})} \qquad (5)$$

The free energy change for the reaction is

$$\Delta G = \Delta G^{\circ} + RT\ln K \qquad (6)$$

Applying the Nernst equation and substituting for $RT\ln K$, $RT\ln a_V$ Eq. 6 becomes

$$\Delta G = -nFE = \Delta G^{o} \; RT\ln a_V$$

where F is the Faraday constant, n is the number of electrons transferred in the reaction (Eq. 5) and E is the electromotive force that is obtained from the cell.

The activity of vanadium is given by

$$a_V = \exp -\left(\frac{nFE}{RT} + \frac{\Delta G^{o}}{RT}\right) \qquad (7)$$

The calculation of $\Delta G^{o}/RT$ in this technique also requires the thermodynamic data for components of Eq. 5 that are listed in Table 2.1.

II. EXPERIMENTAL PROCEDURES

A. Sample Fabrication and Characterization for Oxide Equilibria

1. Introduction. The high vacuum furnaces, the hot press, the optical and x-ray diffraction techniques that were used in these experiments have been described in Part 1. Additional methods and characterization and sample preparation used for the oxide equilibria and the cell experiments will be discussed below.

2. Starting materials: vanadium oxides. The samples for the ternary phase diagrams were prepared from stock powders of metals and metal oxides, except the vanadium oxides. Vanadium oxides are very susceptible to oxidation. Stock powders of these oxides that were not freshly prepared could not be used. All vanadium oxides were prepared as needed except V_2O_5, which was supplied by Cerac Corp. V_2O_3 was synthesized by the reduction of V_2O_5 with hydrogen. High purity hydrogen that was further purified through a Matheson H_2 Purifier was passed over vanadium pentoxide at the rate of 15 cc/min, at 590 °C for 6

h and at 900 °C for 2 h. V_2O_5 was contained in an alumina crucible located in the middle of a vertical Inconel furnace that was evacuated to 0.02 torr and back-filled with nitrogen. The hydrogen flow and the temperature ramping rate were monitored with a Honeywell programmable controller. The resulting black solids were further heated under 1/2 atm. of H_2 until constant weights were obtained. V_2O_3 was characterized by gravimetry (weight loss of V_2O_5) and x-ray diffraction. The vanadium monoxide was prepared by heating pressed pellets of stoichiometric mixtures of vanadium powder and V_2O_3 at 1100 °C for several days. V_3O_5 was similarly prepared by heating equimolar amounts of VO_2 and V_2O_3 for 3 days at 1000 °C. The lower oxides of vanadium V_4O and V_2O were prepared by combinations of the appropriate amounts of vanadium and V_2O_3 at 1000 to 1100 °C and in the presence of $V_{(Pd)}$ alloys. All materials were checked with x-ray diffraction.

The VO phase has the NaCl structure with an extended homogeneous range.[2-3] The composition range of VO is between $VO_{0.76}$ and $VO_{1.3}$, and the lattice constant varies from 4.062 to 4.125.[4] V_2O_3 has the rhombohedral Al_2O_3 corundum structure[5] in which the oxygens form a pseudo-hexagonal close-packing with the vanadium cations occupying two-thirds of the octahedral sites. The reported unit cell dimensions are a = 5.467 Å and α = 53.74°. V_3O_5 has a monoclinic structure and VO_2 is a monoclinic deformation of the rutile structure.[6] V_2O has a monoclinic unit cell[7] which is a distorted version of the tetragonal V_4O unit cell.[4,8] V_4O has a homogeneous range extending between $VO_{0.14}$ and $VO_{0.32}$. The homogeneity-limits of V_2O are $VO_{0.385}$ and $VO_{0.52}$. Wold and coworkers[9] have recently reported that oxidized V_2O_3 contained V_3O_5 and that V_3O_5 can become an integral part of the corundum structure. This

finding is very important to this study because V_2O_3-V_3O_5 binary phases will exhibit different thermodynamic behavior than the single phases.

The freshly prepared oxides were ball-milled to very fine powders and were put through different sized stainless steel classifier screens to separate the different particle sizes. The noble metal powders were separated according to particle size using this method. This screening process was also used to exclude agglomerates that could contribute to large phase separations in the sample. The metal and oxide powders were weighed to one-hundredth of a milligram, mixed thoroughly, and cold-pressed into 13 mm diameter and 3 mm high cylindrical pellets. Table 2.2 lists the source of the starting materials and their specifications.

3. Hot-pressing and annealing. The pressed pellets were hot-pressed following the procedure described in Section 1. The samples were always surrounded by boron nitride powders to prevent reaction of the sample with the graphite dies when the sample was hot-pressed. The samples were initially degassed at low temperatures and high vacuum for 15 to 30 min in the hot press. Partial sintering without pressure at 900 °C for 10 min was necessary to avoid cracking the sample. Complete reaction and sintering occurred at temperatures above 1000 °C and at a pressure range of 300 to 350 atm. depending on the oxide-alloy system. The duration of the reaction also varied from system to system. The samples were allowed to cool under vacuum for several hours. The boron nitride was found not to sinter or react with the various components of the sample. The bulk of the BN protective coating readily separated from the sample upon removal from the reaction container. A few remaining BN particles were removed by ultrasonic cleaning of the sample in ethanol. The outside of the pellets were polished with silicon

carbide paper to remove surface contamination. They were ultrasonically cleaned and dried under vacuum, then weighed and annealed at 1000-1100 °C under high vacuum in alumina crucibles. The crucibles, which had been baked out previously under vacuum at 1700 °C, were covered with tungsten sheets to avoid any possible reaction of Al_2O_3 with the samples. The heat treatments lasted anywhere from 1 to 3 weeks depending on the particle size of the noble metal and the diffusivities of the various metal components.

The heat treatments were frequently interrupted to check with x-rays the number of phases present and the characteristics of the diffraction peaks. X-ray emission line scans across the metallic grains were performed in the scanning electron microscope to see if there was any significant variation in concentration of their constituent elements. When a constant composition throughout the grain was found and the number of phases obeyed the phase rule and the x-ray peaks were sharp, well-defined and all accounted for, equilibrium was almost attained. If additional heat treatments showed no changes in the composition or the x-ray diffraction patterns, the samples were considered fully equilibrated.

4. Alloy preparation. To accurately analyze the binary alloys formed in the equilibration experiment, several standard alloys of known composition were prepared and analyzed. The weighed amounts of the starting materials (usually ingots, rods or sheets of stock materials) were arc melted in a water-cooled copper hearth with a tungsten probe in an inert Ti gettered atmosphere. Each sample was turned over and remelted several times to ensure homogeneous mixing. The arc melted alloy buttons were checked for weight losses and were heat treated for

several hours at 200 to 300 °C below their melting points. SEM and optical characterization indicated that the arc melting and annealing had produced homogeneous products. The results of the preparation and analyses of the standard alloys are presented in Table 2.3 and 2.4.

5. Sample analysis. To prepare specimens for microscopic examination and quantitative analysis, the alloy buttons and the oxide alloy discs were cut into 2 mm-thick slices with a diamond blade saw lubricated by kerosene. The slices were mounted in a Buehler Pneunet mounting press with their flat side exposed. The mounting material was a phenolic resin that contained small particles of amorphous carbon to make the material conducting and remove any charge build up on the samples by the electron beam of the SEM. The mounted samples were polished using several grit sizes of silicon carbide paper. To obtain smooth surfaces for the optical microscope study, additional polishing was performed on an 8" rotating wheel that was covered with a nylon polishing cloth. Diamond paste of 8, 1 and 0.5 μ size was used as the polishing material on the cloth surface and kerosene as the lubricant.

The elemental composition of the alloy grains was obtained by using dispersive energy x-ray analysis EDAX in the scanning electron microscope. In the initial stages of this study the microscope used for the analyses was made by the AMR corporation. It was equipped with a drifted lithium-silicon x-ray detector made by Kervex Corporation. More recently a newer and more accurate WB-G microscope made by International Scientific Instruments Inc. was used. This instrument was equipped with an Ortec 5,000 berillium detector. The characteristic x-ray spectra of the elements present were obtained from 0 to 10 kev with a resolution of 10 eV per channel. The x-ray spectrum of vanadium and rhodium obtained

from a V-Rh-O sample is shown in Fig. 2.2. The silicon escape peaks and the Bremstrahlung radiation were subtracted from the spectra using Quantex Ray software. The software provided the normalized atomic percent composition by integrating the characteristic x-ray peak for each element and using experimentally determined scattering cross sections. However, for most of the binary alloys examined a set of standards of known composition was used to obtain a more accurate composition of the unknown alloys. The absolute intensity of the characteristic x-ray lines of each component of the standard samples was measured.

Cima[10] developed a method based on the Ziebold and Ogilvie technique for determining calibration curves for multicomponent alloys. The one parameter equation that Cima derived relates the relative intensity (R_A) of component A to its mole fraction (X_A) and the mole fraction of component B (X_B).

$$R_a = \frac{X_A\,(a_{BA}X_A + X_B)}{X_A(a_{BA}X_A + X_B) + \lambda X_B(a_{AB}X_B + X_A)} \qquad (8)$$

A_{BA} is a constant which depends on experimental parameters such as the spectrometer tilt angle and the electron beam voltage, and also the mass absorption coefficient for characteristic peaks and the wavelength of the absorption edge of element A and B.

The only unknown parameter in Eq. 8 is λ. The relative intensity R_A is also defined in terms of the absolute intensities obtained from the standards.

$$R_A = \frac{I_A}{I_A + I_B} \qquad (9)$$

A solution of Eq. 9 and a least-squares fit using the different R_A, X_A and X_B data provides the value for λ. A standard plot of R_A versus mole

fraction of A can then be constructed. The relative intensity R_A of element A for an unknown A_xB_y is calculated from the absolute intensities obtained from the EDAX analysis using Eq. 9. The corresponding mole fraction X_A is then obtained from the standard plot. The plots of the mole fraction X_V versus the relative intensity R_V for vanadium-rhodium and vanadium-palladium are presented in Figs. 2.3 and 2.4.

B. Galvanic Cell Experiments

1. Purpose. It was found from the oxide equilibria that the concentration of vanadium in the V-Pd alloy in equilibrium with V_2O_3 and V_3O_5 at 1000 °C is approximately 0.5%. This particular concentration is very important for the V-Pd system because it fixes the upper limit of its titration curve. It is also very uncertain because it is very near the detection limit of the analytical instrument (± 0.03%). To check this finding, solid state electrochemical cells were used to examine the thermodynamics of alloys that contained 1.1-1.3% vanadium. The cells, which were of the type described in the theoretical section, will be used in future work to complete the titration curve.

2. Electrolyte operation and Preparation. The cells depend on the fact that the electrolyte conducts oxygen anions. Compounds which exhibit oxygen ion conduction are found among the oxides of quatravalent metals that have the fluorite structure (ZrO_2, ThO_2, HfO_2). Solid solutions of this oxides with oxides of lower valent cations (Ca^{2+}, Y^{3+}) at concentration of 10-20% retain the fluorite structure. The introduction of these cations in the fluorite structure results in the formation of oxygen defects to maintain charge neutrality.

Oxygen anion conduction occurs through these defects. The electrolytes used in this study were a solid solution of 85 mol % ThO_2

and 15 mol % $YO_{1.5}$. This composition has been found to give maximum ionic conductivity.[1-2] Also the ThO_2 based electrolytes cannot be reduced as easily as other ionic conductors. Thus, they can maintain ionic conductivity when used in highly reducing systems.

The electrolytes were prepared from mixed ThO_2 and Y_2O_3 stock powders. In a glove box, to contain any radioactivity, the mixed powders were pressed into pellets of 12 mm diameter and 3 or 4 mm thickness. To eliminate contamination of the electrolytes a special high vacuum furnace with a tungsten mesh filament and high purity, molybdenum heat shields was used for the sintering of the thoria-yittria pellets. Impurities such as carbon and polyvalent metals increase the electronic conductivity and eventually destroy their performance. The pressed pellets were placed on the sharp tips of 6 vertical tungsten pins supported on a cylindrical molybdenum disc. This arrangement minimized the contact of the sample with the sample holder to a few small spots. The samples were fired for 45 min or 1 h at 2000 °C in 500 torr of high purity H_2 to yield a white, dense solid solution of ThO_2/Y_2O_3. The furnace was heated at a slow rate of 140 °C per h and was cooled at the same rate in order to avoid thermal shock cracking of the specimens. Hydrogen was used as the sintering gas. Because of its smaller atom size, hydrogen can readily escape from the lattice. Hydrogen also assists shrinkage of pores which would yield high density electrolytes that are needed to obtain satisfactory EMF results. Sintering periods longer than 1 h at 2000 °C yielded dark gray or black samples because presumably the hydrogen was reducing ThO_2. The colored samples regained their white color after heated in air at 1000 °C for 24 h. The electrolytes were polished with 600 grit silicon carbide paper.

3. Electrode fabrication and manipulation. The V_2O_3-$V_{(Pd)}$ electrode was prepared from 45 to 55 wt % mixtures of vanadium-palladium alloy and V_2O_3 powder. The sample was pressed into pellets and equilibrated at 1000 °C for 7 days. The reference electrodes were made from a 1:1 weight mixture of tantalum and tantalum pentoxide powders pressed into pellets and homogenized in vacuum at 1200 °C for 4 to 7 days. Ta-Ta_2O_5 was selected as a reference electrode because of its low oxygen partial pressure and its good reversibility. The surfaces of the electrodes were mechanically polished using 400 to 600 silicon carbide paper to insure intimate interfacial contacts. The samples were ultrasonically cleaned in alcohol, dried, and x-rayed to identify the phases present. The cell was assembled with great care not to contaminate the components with impurities that could cause erroneous EMF measurements. All the ceramic parts that make up the cell system discussed below were heated at 900 °C in air to remove carbon impurities. Prior to their use, the metallic parts were cleaned and baked under vacuum. Materials and parts were handled with clean surgical gloves. The electrode-electrolyte-electrode cell pellets were sandwiched between two alumina discs, were compressed with tantalum bolts to keep the pellets in close contact, and were annealed at 1000 °C for 1 day to equilibrate the contacting surfaces.

4. Apparatus. The experimental procedure and the equipment for the cell study is substantially similar to those of earlier studies by Cima[10] and Bullard.[11] A schematic diagram of the cell apparatus is shown in Fig. 2.5. The cell chamber was a vertical Inconel tube (2" inner dia. and 24" length) enclosed at the bottom end. A brass compression fitting with a Vitron O-ring was inserted at the top end.

The fitting supported a Conflat flange on which the end cap flange of the chamber was bolted making a leak-tight seal with a Vitron O-ring. The top end of the vertical alumina rod that carried the cell assembly at its bottom end was attached to the end cap. The cell assembly was held firmly against the support rod with a spring-pressure mechanism. The mechanism consisted of two alumina tension rods which were connected to the cap flange with stainless steel springs. The other end of the rod was firmly connected to an alumina disc with tantalum screws. The cell assembly was compressed between the alumina discs and the support rod by the tension rods. The compressive force was provided by the springs. The platinum wires used to carry the EMF of the cell were inserted in alumina sleeves that brought them down to the cell. There they were spot-welded to the platinum contact discs. A Pt-Rh (10% Rh) thermocouple was placed within a centimeter of the cell to measure the temperature. The cell assembly consisted of the electrolyte surrounded by the electrodes and the Pt contacts. All these components were held in place between two alumina discs bolted together with Ta screws. The screws were removed once the spring loading system was in place. Spacer pellets were often inserted between the top discs of the cell assembly and the disc that held the tension rods to correct for the variation in thickness at the different cells.

During an experimental run the Inconel chamber containing the assembled cell system was inserted in a 76 cm three-zone furnace. Separate power supplies (Eurotherm Corp.) provided power to the three Kanthal wire wound furnace zones. The controllers of the power supplies kept a constant temperature for a 12" range in the center section of the furnace. The temperature settings were controlled by an IBM-PC com-

puter. The furnace was heated slowly to 600 °C at a rate of 100 °C/h under dynamic vacuum to degas the chamber and the components of the cell system. Pure helium was used to flush the chamber and maintain an inert atmosphere during the run. High purity He (purity: 99.999%) was further purified by passing it through a liquid nitrogen trap to remove any condensible impurities. After the cold traps, the gas flowed through an Inconel tube containing zirconium getters that were heated with two separate furnaces at 900 °C and 600 °C to remove methane or oxygen contaminants. Finally, the helium was brought to the bottom of the cell chamber through a tantalum tube which was connected to the gettering system with a stainless steel flexible hose with a Nupro valve. The helium went through another gettering container packed with zirconium foil, over the cell, to a rotometer and exited to a mechanical pump through a throttle valve. The rotometer was used to control the gas flow rate in the cell. Additional zirconium gettering foil surrounded the cell to remove any residual oxygen or other gases which may arise from degassing of the chamber walls. The cell EMF was measured using a Keathley Model 610 potentiometric electrometer with a minimum input impedance of 10^{14} ohms. The output signal was displayed in millivolts on the deflection scale of the potentiometer. the data were collected and stored in an IBM-PC with software written by Bart Ebbinghaus.

5. Cell operation. After the cell was degassed at 600 °C the purified He was introduced and the temperature was raised to 875 °C using the computer operated controllers. The cell was allowed to equialibrate at this temperature for 4 to 6 h. Equilibrium was considered to have been obtained when the EMF was constant to within 1 mV. The temperature was raised to 950 °C and the cell was allowed to

reequilibrate at this temperature for a few hours. When a steady EMF was obtained, the temperature was ramped by 25 to 50 °C to a new point and the equilibration-data collection process was repeated. A typical ramp rate between temperatures was 2.5 °C per min The EMF's were checked for reproducibility by varying the temperature and comparing the EMF's obtained with those measured previously for the same temperature point. All temperature points were preset using the Ebbinghaus software. The durations of the cell experiment were from 2 to 4 days.

These experiments are susceptible to various systematic errors. Several tests were performed to check the validity of the results. Reversibility was checked by shorting the cell for several minutes. The shorting causes a large variation in the EMF which was restored to its original value within a few hours. Change of the inert gas flow rates was used to check for variation in the measured EMF. Variation of the EMF with flow rate indicates poor contacts of the electrode with the electrolyte or the presence of gaseous impurities such as CO or O_2. Experiments in which there was change in the EMF with flow rates were discarded. Diffraction patterns of the interfaces of the electrodes and the electrolyte were obtained to check that no side reactions had occurred during the run.

III. REFERENCES

1. L. Brewer, B. Ebbinghaus, Thermochimica Acta (in press).
2. R. Tetot, C. Picard, J. Solid State Chem. **66**, 324-31 (1987).
3. R. Tetot, C. Picard, R. Gerdanian, J. Solid State Chem. **68**, 88-93 (1987).
4. N. Shönberg, Acta Chemica Scand. **8**, 221-25 (1954).

5 G. Anderson, Acta Chemica Scand. **8**, 599 (1954).

6. G. Anderson, Acta Chemica Scand. **10**, 623-28 (1956).

7. S. Westman, Acta Chemica Scand. **17**, 749 (1963).

8. M. Cambini, G. Pellegrini, S. Aemlinkx, Mat. Res. Bull. **6**, 791, 804 (1971).

9. N. L. Gray, R. Kershaw, W. Croft, K. Dwight, A. Wold, J. Solid State Chem. **62**, 57-63 (1986).

10. M. J. Cima, Ph.D. dissertation, Univ. Calif., Berkeley, 1986.

12. G. Bullard, Ph.D. dissertation, Univ. Calif., Berkeley, 1976.

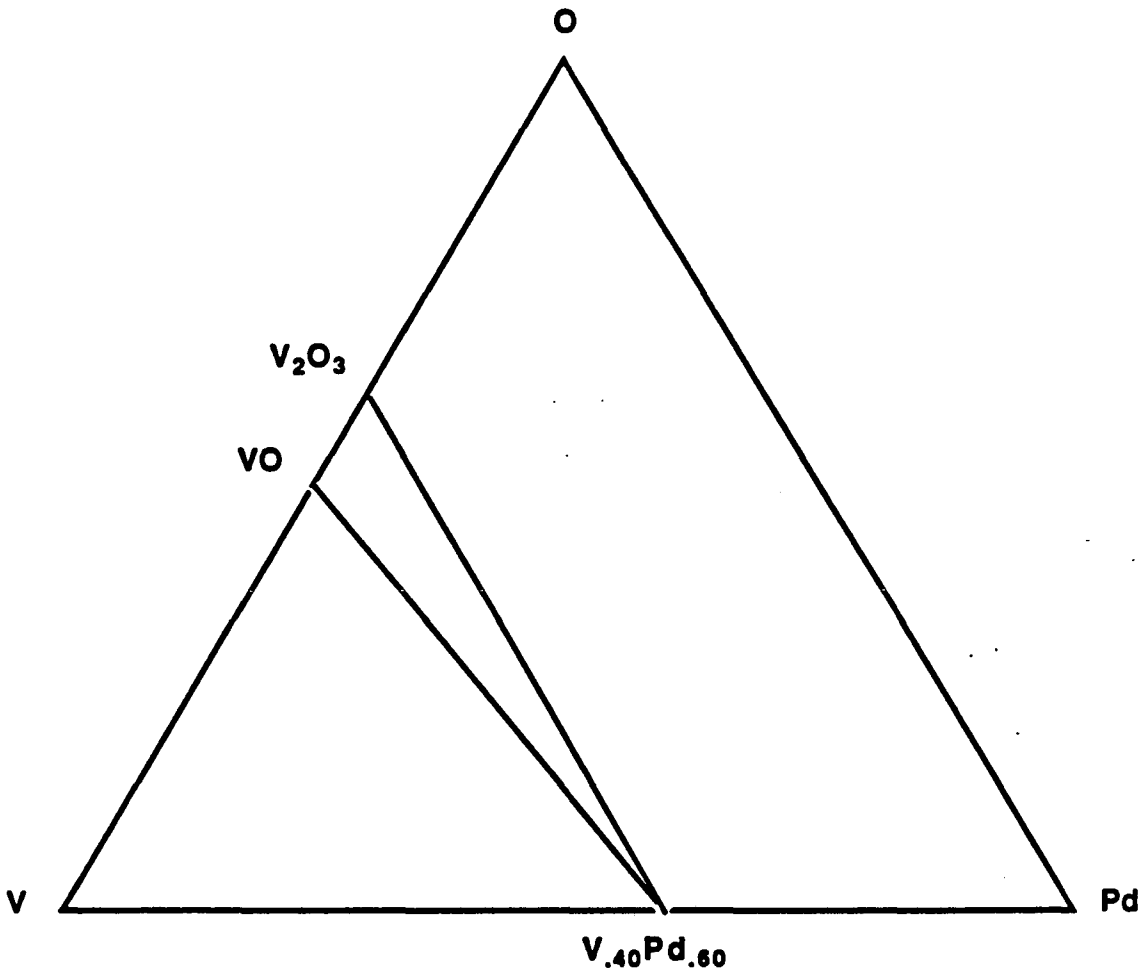

FIG. 2.1. The partial V, O and Pd ternary diagram. In the VO, V_2O_3 and $V_{0.40}Pd_{0.60}$ three-phase region the activity of vanadium is equal in all three compounds.

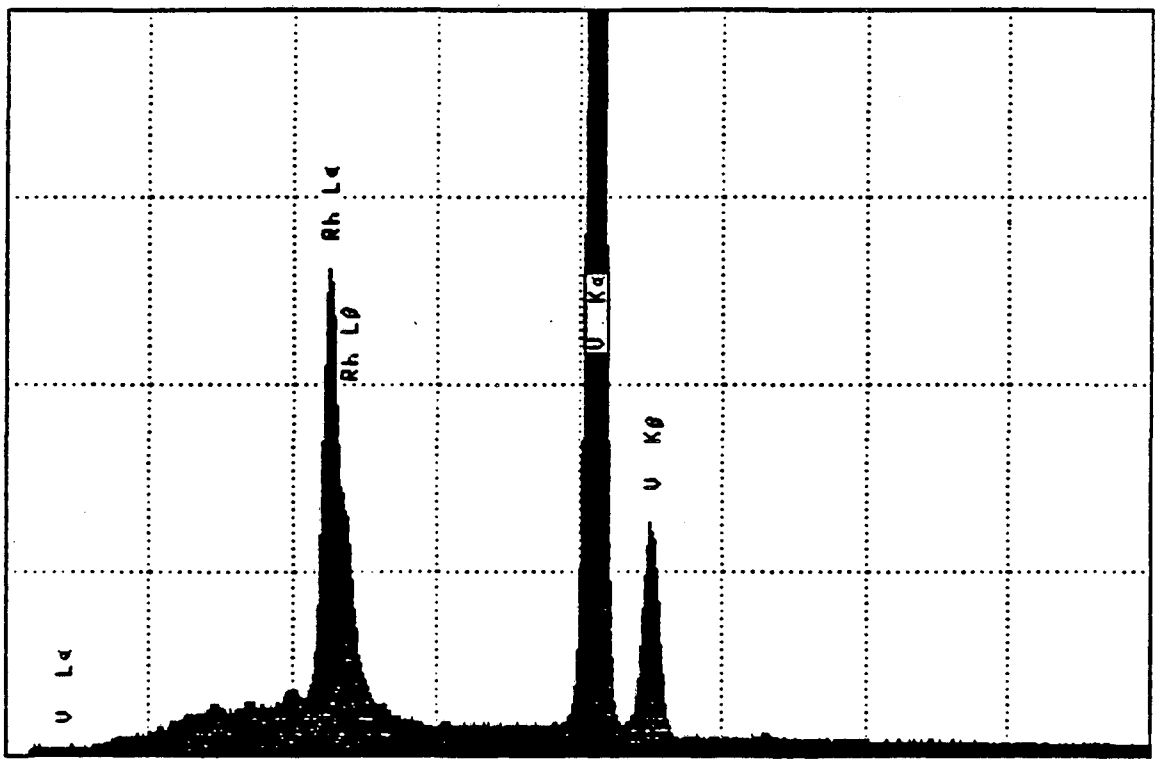

FIG. 2.2. The x-ray spectrum of a vanadium-rhodium sample. The vanadium K(α) and the rhodium L(α) lines are used for quantitative microanalysis.

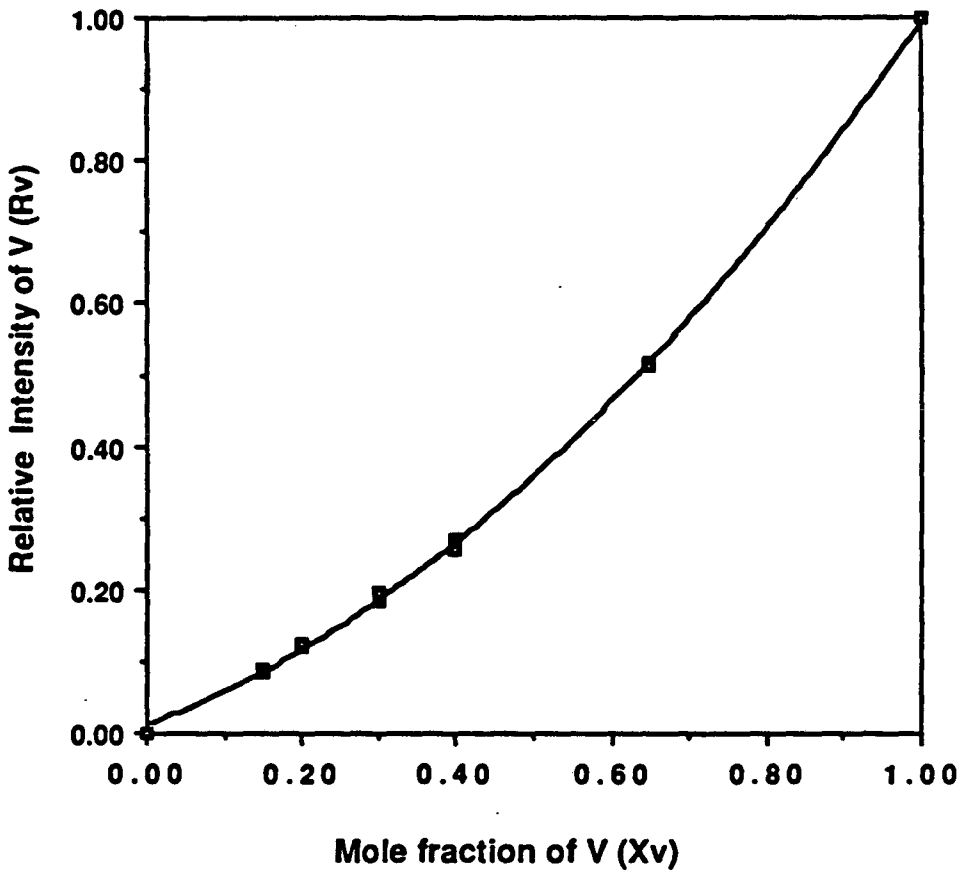

FIG 2.3. The relative intensity (Rv) of the V(Kα) and Pd(Lα) x-ray lines as a function of the mole fraction (Xv) in the standard V-Pd alloys.

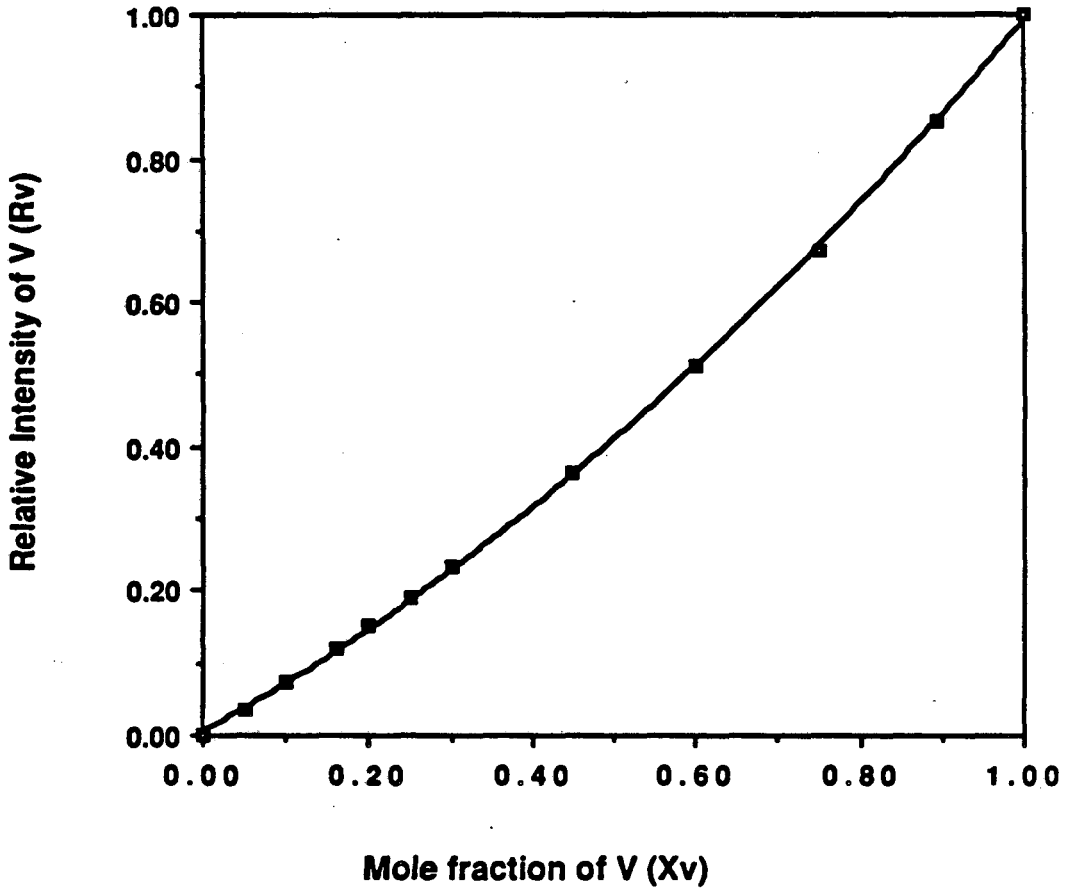

FIG 2.4. The relative intenstiy of V(Kα) and Pd(Lα) x-ray lines as a function of mole fraction (Xv) in the standard V-Rh alloys.

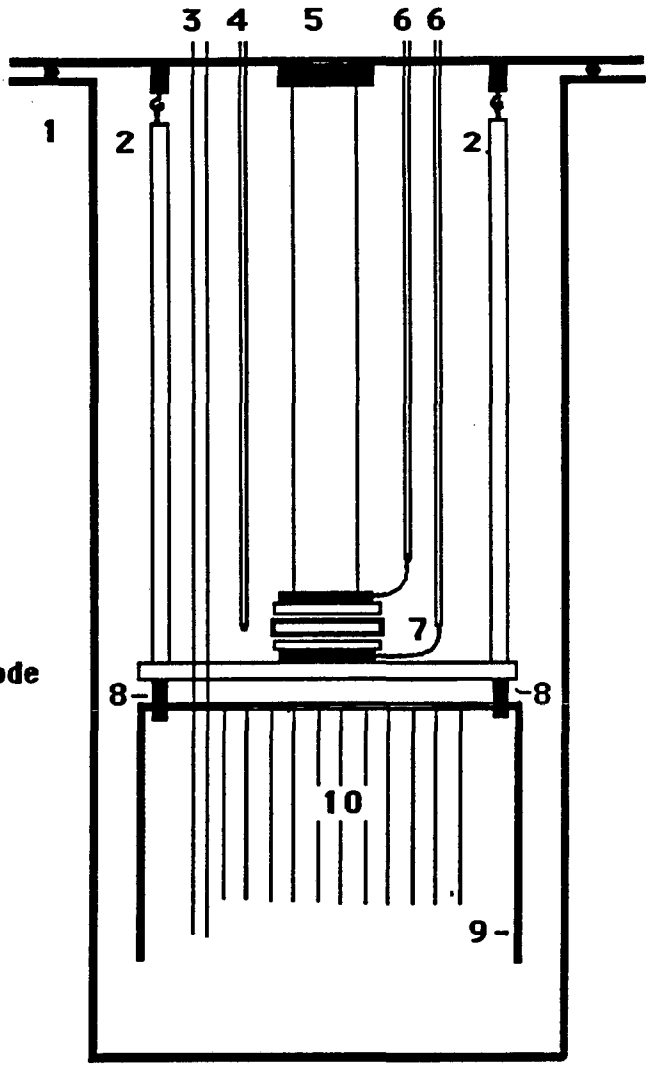

1. inconel tube
2. tension rod
3. helium flow tube
4. thermocouple
5. support rod
6. emf lids
7. cell assembly
   (Pt disc, electrode,
   electrolyte,electrode
   Pt disc)
8. Ta screws
9. Zr getter chamber
10. Zr sheets

FIG. 2.5. Schematic diagram of the cell apparatus.

TABLE 2.1. Vanadium oxides

	$-(G^{o}-H^{o}_{298})/RT$ at 1000 °C	$-\Delta G_f/R$ (kK) 1000°C	$-\Delta H_{f298}/R$ (kK)
V	5.6418	0	0
$VO_{1/4}$		10.9974	
$VO_{1/2}$		20.1521	
VO	8.3343	38.0091	51.927
$VO_{3/2}$	10.6831	53.690	73.291
$VO_{5/3}$	11.4616	56.343	77.728

TABLE 2.2. Starting materials.

Material	Supplies	Purity %	Particle size
V	Cerac	99.5	-325 mesh
Ti	Alfa	99.0	-100 mesh
Nb	Cerac	99.5	-325 mesh
Pd	Alfa	99.9	-60 mesh
Pd	Johnson Mathey	99.9	0.2-0.3 μ
Pd	LLNL stock	--	0.030" sheet
Rh	LLNL stock	--	-400 mesh
Rh	LLNL stock	--	0.030 sheet
Pt	Alfa	99.9	-60 mesh
Pt	Aesar	99.9	0.5-2.5 μ
Ir	Apache	99.8	-400 mesh
Ta	Aesar	99.98	-325 mesh
VO	Cerac	99.5	-80 mesh
V_2O_5	Cerac	99.9	-200 mesh
Ta_2O_5	Cerac	99.5	-325 mesh
Y_2O_3	Cerac	99.9	-325 mesh
TiO_2	Cerac	99.9	-325 mesh
Nb_2O	Cerac	99.9	-325 mesh
NbO	Cerac	99.8	-100 mesh
NbO	Cerac	99.9	-200 mesh

TABLE 2.3a. V-Pd arc melted standards.

Sample ID	at% Pd	at% V	Annealing Temp. °C	%Weight Change
V1	90.17	9.83	1100 14 h	-19.84
V2	84.61	15.39	1100 2 h	-0.96
V3	79.66	20.34	1100 2 h	-1.06
V4	74.92	25.08	1100 14 h	-7.54
V5	69.81	30.19	1100 2 h	-0.78
V6	59.96	40.04	1100 2 h	-0.13
V7	50.02	49.98	1100 14 h	+0.59
V8	35.00	65.00	1100 2 h	-0.22
V9	25.12	74.88	1100 14 h	-0.64
V10	10.04	89.96	1100 14 h	+4.42

The samples annealed for 14 h show significant weight losses and gains. The losses were probably due to vaporization. The gains were due to deposition of vaporization products. Only the samples annealed for 2 h that show normal weight charge were used to construct the standard curve.

TABLE 2.3b. V-Rh arc melted standards.

Sample ID	at% Rh	at% V	Annealing Temp. °C	%Weight Change
VR1	94.67	5.33	1000 12 h	--
VR2	89.93	10.07	1000 12 h	0.94
VR3	84.15	15.85	1000 12 h	0.91
VR4	79.93	20.07	1000 12 h	--
VR5	74.64	25.36	1000 12 h	0.72
VR6	70.26	29.74	1000 12 h	--
VR7	54.78	45.22	1000 12 h	0.55
VR8	40.49	59.91	1000 12 h	0.45
VR9	25.81	74.19	1000 12 h	--
VR10	10.46	89.46	1000 12 h	--

TABLE 2.4a. EDAX analysis of V-Pd standards.

Sample ID	V(Kα)	Pd(Lα) Intensity (CPS)	R_V	X_V average
V2	8.667	88.40	0.089	0.15
	9.477	100.30	0.086	
	10.54	112.5	0.086	
V3	5.080	36.52	0.122	0.20
	5.263	38.54	0.120	
	5.840	40.70	0.125	
V5	23.16	99.07	0.189	0.30
	15.95	69.30	0.187	
	15.27	67.17	0.185	
V6	24.78	68.34	0.266	0.40
	24.96	72.25	0.257	
	17.53	47.45	0.270	
V8	51.17	48.11	0.515	0.65
	64.59	60.14	0.517	
	69.26	66.21	0.511	

TABLE 2.4b. EDAX analysis of V-Rh standards.

Sample ID	V(Kα)	Rh(Lα) Intensity	R_V (CPS)	X_V average
VR1	1.157	29.40	0.038	0.053
	1.367	33.78	0.039	
	1.507	38.55	0.038	
VR2	3.927	51.72	0.071	0.100
	4.987	61.37	0.075	
	5.720	72.03	0.074	
VR3	3.190	24.42	0.116	0.159
	3.833	30.82	0.111	
	4.953	36.11	0.121	
VR4	2.400	13.30	0.153	0.201
	3.737	20.90	0.152	
VR5	40.34	17.85	0.184	0.254
	40.59	178.3	0.185	
	34.52	155.7	0.182	
VR6	47.19	167.7	0.220	0.297
	42.19	149.8	0.220	
	47.25	169.3	0.218	
VR7	94.10	170.3	0.356	0.452
	68.64q	121.2	0.362	
	67.43	120.0	0.360	
VR8	167.6	158.6	0.514	0.599
	171.9	165.3	0.510	
	167.1	160.2	0.511	
VR9	274.4	134.6	0.671	0.742
	274.9	131.1	0.677	
	280.3	136.0	0.673	
VR10	265.0	40.99	0.866	0.895
	272.1	40.50	0.870	
	267.1	39.56	0.871	

PART 2. SECTION 3: RESULTS AND CONCLUSIONS

I. VANADIUM OXIDE-PLATINUM GROUP METALS EQUILIBRIA

A. Introduction

This section deals primarily with the derivation of the ternary-phase diagram of Pd-V-O and a limited study of the corresponding Rh and Ir diagrams at 1000 °C. The sample preparation was guided by the V-O,[1,2] V-Pd,[3,4] V-Rh,[5,6] and V-Ir[7,8] binary systems. The V-Pd system was initially investigated by Köster and Haehl.[3] Their phase diagram was reexamined by Waterstrat[4] at a temperature range of 700-900 °C to confirm the existence of three ordered phases. The portion of the diagram that directly applies to this study is at 1000 °C and across the entire compositional range. It consists of a homogeneous range of the fcc Pd structure and the bcc vanadium structure with a miscibility gap in between (Fig. 3.1). The V-O system, briefly discussed in previous sections, is dominated by a large number of refractory phases, stable up to their melting points and extending from the solid solution of oxygen in vanadium to the distorted rutile VO_2 phase. The phases higher in oxygen content than VO_2 melt or decompose below 1000 °C and are not suitable for this study.

B. V-Pd-O Equilibria

The V-Pd-O samples used for this phase study are listed in Tables 3.1 and 3.2. All samples were examined by diffraction, optical, and microscopic techniques. They proved to be composites of two or three binary phases. There were no indications of ternary $V_xPd_yO_z$ phases. The binary phases were vanadium oxides and vanadium-palladium alloys. Figure 3.2 shows an electron micrograph obtained from a polished

specimen of sample VPd6. The multiple phases can be easily distinguished by the difference in brightness. The brightest grains belong to a metallic phase containing an excess of palladium. The next in brightness belongs to a V-Pd phase with less palladium content. The dark grain is part of the VO_x oxide phase. In situ microprobe analysis also distinguished intermetallic and oxide grains. X-ray powder data confirmed the presence of the three phases. Since the temperature and pressure are fixed, the phase rule allows only three phases at equilibrium and that is precisely what is observed in this sample.

Figure 3.3 is an electron micrograph of sample VPd7. It contains a phase of metallic luster and a dark-gray oxide phase. Microanalysis confirms the presence of vanadium and palladium in the bright grain, and only vanadium in the dark grains. The x-ray diffraction pattern (Fig. 3.4) clearly reveals the presence of the fcc Pd-V solution, the sodium chloride-like VO phase, and the corundum V_2O_3 phase. The electron image cannot resolve the two oxide phases. Careful examination of a polished specimen of this sample in an optical microscope with unpolarized light shows two kinds of oxide grains in addition to the alloy grains. Optical microscopy has proved to be very useful in determining the number of grains in oxide phases having very complex or similar diffraction patterns, such as the Magnelli phases.

X-ray dispersive analysis line scans are also illustrated in Fig. 3.3. The top line across the metallic grain represents the intensity of the palladium L(α) x-rays emitted as the microprobe traces the solid white line across the sample. The bottom line represents the intensity of the V L(α) x-ray. The small variation of the x-ray intensities indicates that the vanadium and palladium concentrations are constant

across the grain. Several such line scans were performed on other grains to show that the sample is homogeneous throughout, and that the only heavy elements present are vanadium and palladium. This method of analysis cannot detect light elements such as oxygen and carbon that would contribute s,p electron density and greatly alter the electronic structure of the alloys. Large solubility of oxygen in the metallic grains or palladium solubility in the oxide phases also cannot be detected with this method. Auger electron spectroscopy, accompanied by argon ion sputtering performed on selected samples, did not reveal any significant presence of oxygen in the metallic phases or palladium in the oxide phases. Auger analysis examples will be presented below when the Nb-Pt-O system is discussed. Although the Auger analysis was limited to only a few samples, the V-Pd-O diagram and all the other ternary systems that follow are constructed on the assumption that ternary phases are not formed in these experiments. A careful x-ray data analysis of each sample used did not show any indications of ternary phases.

The equilibrium conditions in the V-Pd-O system were checked by varying the particle size of palladium or repeating a particular experiment with different starting materials. Samples VPd2 and VPd3 listed in Table 3.2 have the same initial compositions and starting materials, however, the particle size of Pd metal is different in each. Sample VPd2 contained 1-3 μ size Pd and required 4 to 6 days to homogenize. Sample VPd3 contained 200 μ size Pd and required several weeks to reach equilibrium. In both samples the composition of the alloy was the same. The V-Pd-O diagram was determined by using palladium powder 3 μ in size. The reproducibility of the composition of

the alloy in the oxide equilibria experiments was often checked by varying the compositions of the starting materials or selecting different starting materials. Samples VPd7 and VPd8 from Table 3.2 are examples of the varied compositions used in this study. Sample VPd7 contains VO, V_2O_3 and a Pd-V alloy when equilibrated. The relative proportions of VO and V_2O_3 as shown by its powder pattern are similar. The amount of vanadium in the alloy is 39.5 atomic percent. It was prepared from a V_2O_3, V and Pd mixture. Sample VPd8 contains a large amount of VO, traces of V_2O_3 and a V-Pd alloy. The V atomic composition is 38.5 percent. This sample was prepared from V_2O_3, VO, V and Pd. Although the proportions of the equilibrium oxide phase vary significantly from sample to sample, and their starting materials were quite different, the alloy composition appears to be very consistent. This finding demonstrates that if an initial composition is within the boundaries of the VO-V_2O_3-$V_{0.39}Pd_{0.41}$ region, the resulting alloy will be independent of its initial components and the proportion of the equilibrium oxides. Similar reproducibility was observed among other samples of the V-Pd-O system.

The only discrepancy encountered in this system was observed in sample 73A. Its equilibrium products were V_4O, V_2O and $V_{0.74}Pd_{0.245}$. This vanadium composition, however, should fall in the miscibility gap of the V-Pd binary system. The vanadium boundary, as shown in Fig. 3.1, changes very rapidly with temperature. A temperature error of 25 to 50 °C could easily place this alloy composition in the V homogeneous region. Furthermore, this vanadium boundary may have been incorrectly estimated by Köster. A summary of the preparation and characterization

of the V-Pd-O samples is given in Table 3.1. In Fig. 3.5 the V-Pd-O phase diagram is presented as derived from the samples listed in Table 3.2.

C. V-Rh-O Equilibria

In the V-O-Rh system only the VO-V_2O_3, V_2O-VO and V_4O-V_2O ternary regions were investigated. A VO-V_2O_3-Rh mixture required 18 days at 1000 °C to reach equilibrium. This is partly due to the slow diffusivity of vanadium in rhodium (rhodium is bonded more tightly than palladium) and partly due to the larger particle size (45 μ) of rhodium metal used in these experiments. The mole fraction of vanadium in the resulting alloy was 0.485. X-ray diffraction confirmed the presence of the α_3-VRh phase which is isomorphous to the α-VIr structure. This is an orthorhombic distortion of the CsCl structure. The x-ray powder pattern (Fig. 3.6) also included the VO and V_2O_3 phases. The x-ray data for the α_3-V-Rh phase are listed in Table 3.3. The V_2O-VO and V_4O-V_2O ternary regions were found to be in equilibrium with a vanadium-rhodium solid solution with X_V = 0.85 and X_V = 0.88, respectively. A sample that was prepared with a combination of V_2O_3, VO_2 and Pd resulted in a mixture of two Magnelli phases and palladium with undetected vanadium. This is consistent with the V-Pd-O study (see Table 3.4 and 3.5 for preparations and results of V-O-Rh equilibria).

D. V-Ir-O Equilibria

The regions of interest in the V-Ir-O phase study are the VO-V_2O-IrV_3, VO-V_2O_3-IrV_2, and V_2O_3-(V_3O_5)-$Ir(V)_{ss}$. The IrV_3 phase (25 at. percent Ir) was found in equilibrium with VO and V_2O. The reaction VO with a small amount of iridium at 1000 °C for one week resulted in the formation of the IrV/IrV_3/VO_x mixture ($1<x<1.27$). Additional heating at

1000 °C for 2 weeks yielded V_2O_3 + $VO_{1.27}$ and an iridium vanadium compound with the IrV_3 structure. The concentration of iridium in this phase was 35%. The IrV_3 phase has a very large homogeneous range extending from 22 to 38 at. percent iridium. The reaction of Ir with V_2O_3 and with a mixture of V_2O_3 and V_3O_5 produced an Ir(V) alloy with ~8 at. % vanadium. Optical micrographs at 1000× magnification showed two oxide phases and one alloy phase. Electron microscopy (SEM) also indicated the presence of only one alloy. The x-ray powder pattern clearly showed the alloy phase and V_2O_3 with its reflections somewhat shifted. The V_3O_5 phase is perhaps integrated in the V_2O_3 corundum structure.[12] Small amounts of V_3O_5 or another higher oxide must be present, taking into account the original concentrations of V_2O_3 and Ir for this sample and the significant reaction between these two materials (Table 3.4 and 3.5 for preparations and results of V-Ir-O equilibria).

E. Ti-Ir-O Equilibria

The equilibration of the Ti-Ir-O system was designed to yield the ternary regions of two oxides and an alloy. The appropriate amounts of Ti and Ti_2O_3 were combined so that the resulting composition would lie in the TiO-Ti_2O_3 two-phase region of the binary Ti-O system. Also, Ti_2O_3 and TiO_2 were combined so than the resulting composition would lie in the Ti_2O_3-Ti_3O_5 two-phase region of the binary Ti-O system. A small amount (5%) of iridium was added in the two oxide samples. The samples were heated to 1400 °C ±25 °C for 4 days. Diffusion in iridium is much slower than in Pt or Pd so a higher temperature was selected to reach equilibrium in a reasonable time period. X-ray data showed that the α-TiIr phase[9] was made by reaction of TiO and Ir.

$$3TiO + Ir \longrightarrow Ti_2O_3 + IrTi \qquad \text{(reaction 1)}$$

In addition, $TiIr_3$ was found to form from the reaction of Ti_2O_3 and Ir.

$$5Ti_2O_3 + 3Ir \longrightarrow 3Ti_3O_5 + Ir_3Ti \qquad \text{(reaction 2)}$$

Elemental analysis of the alloy phases confirmed the x-ray findings. The alloy of reaction 1 contained 46 at % Ti and 54 at % Ir, while the alloy of reaction 2 contained 25 at % Ti and 75 at % Ir (see Table 3.6 and 3.7 for preparations and results of Ti-Ir-O equilibria).

F. Nb-Ir-O and Nb-Pt-O Equilibria

Various combinations for NbO_2, Nb_2O_5 and Nb metal were reacted at 1400 °C with Pt and Ir to study the thermodynamic activities of vanadium in certain Nb-Ir and Nb-Pt intermetallics. The ternary region found in these systems are NbO-NbO_2-Nb(Ir), NbO-NbO_2-Nb(Pt) and $Nb_{12}O_{29}$-$NbO_{0.43}$-Pt(Nb). The Nb-Ir alloy in the NbO-NbO_2-NbIr sample contained 34 at. % Nb. This composition is part of the homogeneous range of the σ-phase[10] which extends from 32.5 to 41 at. % Nb. The x-ray data confirmed the existence of the σ-phase in the sample. The intermetallic of niobium-platinum intermetallic in equilibrium with NbO and NbO_2 has not been fully characterized yet. Powder data, however, indicate that it may be the Nb_2Pt phase reported by B. T. Matthias *et al.*[11] The phase in equilibrium with the higher niobium oxides is undoubtedly Pt_3Nb which exhibits a very small homogeneous range of 1-1.5 at %. This sample was studied extensively by Auger spectroscopy to show that there was not any oxygen dissolved in the alloy phases or any platinum dissolved in the oxides. A composition versus depth Auger profile clearly demonstrated the absence of oxygen in the alloy grains. The Auger spectrum of an

alloy grain illustrated in Fig. 3.7 and its composition versus depth profile is shown in Fig. 3.8 (Table 3.6 and 3.7 for preparations and results of Nb-Ir-O and Nb-Pt-O equilibria).

III. THERMODYNAMIC QUANTITIES

A. Oxide Equilibria

From the phase diagram studies that were described in the previous sections the thermodynamic quantities of the alloys that are found to be in equilibrium with a pair of oxide phases can be derived. In the V-Pd phase diagram there are five such alloys. The alloy oxide combinations are the following: V_4O-V_2O-$V_{(Pd)}$, V_2O-VO-$V_{(Pd)}$, VO-V_2O_3-$Pd_{(V)}$, V_2O_3-$V_3O_5Pd_{(V)}$ and V_3O_5-$V_4O_7Pd_{(Pd)}$. The oxide pairs and the compositions of the corresponding alloys are listed in Table 3.1. To begin the calculations, the VO, $V_2O_3V_{(Pd)}$ combination is taken as an example. In this combination the standard Gibbs free energies of the oxides fix the thermodynamic activity of vanadium in the alloy by the the following equation.

$$3VO \longrightarrow 2VO_{3/2} + V_{(Pd)} \qquad \text{(reaction 3)}$$

The values for the Gibbs energy functions $-(G^o - H^o_{298})/RT$ for VO, $VO_{3/2}$ and V are combined for the above equation to yield the change of the Gibbs energy function, $-(\Delta G^o - \Delta H^o_{298})/RT$, for the above reaction. Table 2.1 lists the data needed for this calculation and the subsequent calculations.

$$-(\Delta G^o - \Delta H^o_{298})/RT = 2.005 \qquad (1)$$

The enthalpies of formation are combined to yield the enthalpy change for reaction 3.

$$\Delta H^{o}_{298}/RT = 7.226 \qquad (2)$$

The Gibbs free energy $\Delta G^{o}/RT$ is obtained by combining expressions 1 and 2.

$$\Delta G^{o}/RT = 5.226$$

As described in Section 2, this quantity is related to the activity of vanadium in the following manner.

$$-\Delta G^{o}/RT = \ln a_V$$

$$a_V = 5.40 \times 10^{-3}$$

The activity coefficient is calculated from the ratio of activity and mole fraction.

$$\gamma_V = a_V/X_V = 1.35 \times 10^{-2}$$

$$-\log\gamma_V = 1.87$$

The activities and the activity coefficients for the vanadium in the alloys for the other four combinations are calculated in the same way. The equations used, activities of vanadium in palladium and the corresponding activity coefficients are the following:

Equations	a_V	$-\log\gamma_V$ (1273 K) in Pd	$-\log\gamma_V$ (1273 K) in Rh	$-\log\gamma_V$ (1273 K) in Ir
$2VO_{1/4} \rightarrow VO_{1/2} + V$	2.33×10^{-1}	0.55	0.58	
$2VO_{1/2} \rightarrow VO + V$	2.03×10^{-1}	0.57	0.60	0.57
$3VO \rightarrow 2VO_{3/2} + V$	5.40×10^{-3}	1.87	1.95	2.08
$5V_2O_3 \rightarrow 3V_3O_5 + V$	3.41×10^{-11}	8.2	<8.2	9.37
$7V_3O_5 \rightarrow 5V_4O_7 + V$	9.62×10^{-12}	8.3		

The thermodynamic data for the Ti-Ir and the Nb-Ir alloys were also calculated in the same way as for the V-Pd alloys and are listed below.

Equations	a_{Ti}	$-\log\gamma_{Ti}$ (1673 K) in Ir
$3TiO \rightarrow Ti_2O_3 + Ti$	2.24×10^{-3}	2.32
	1.12×10^{-3}*	2.61
$5Ti_2O_3 \rightarrow 3Ti_3O_5 + Ti$	9.04×10^{-6}	4.42

*The activity of Ti in the TiO-Ti_2O_3 region was corrected for the TiO nonstoichiometry.

Equation	a_{Ti}	$-\log\gamma_{Nb}$ (1673 K) in Ir	$-\log\gamma_{V}$ (1273 K) in Ir	$-\log\gamma_{Nb}$ (1273 K) in Pd[13]
$2NbO \rightarrow NbO_2 + Nb$	5.54×10^{-2}	1.10	1.41	1.26

B. Galvanic Cells

The galvanic cell experiment was used to check the thermodynamic data obtained for very low vanadium concentrations in the V-Pd system. The small amount (0.5% ±0.2%) of vanadium present in the alloy of V_2O_3-V_3O_5 combination is certainly reasonable since it fixes the value of the activity of vanadium at the very low value of near infinite dilution at 3.41×10^{-11}, which is greater than the value derived by Cima for the Nb-Pd system. This is because niobium is a better acid than vanadium and is expected to bond tighter to Pd than would vanadium. To confirm that the 0.5% of vanadium measured is reproducible and not an instrumental error, three samples with oxide compositions intermediate to V_2O_3 and V_3O_5 were prepared from different V-O starting materials and were reacted with Pd metal. Upon equilibration all three samples contained a mixture of the two oxides and Pd metal in which 0.5%-0.6% of vanadium was detected.

The sample that was checked with the cell was prepared from V_2O_3 and a Pd-V solution in which the mole fraction of V was 0.013. This amount can be easily and accurately detected by x-ray dispersive analytical techniques. This sample was homogenized for 1 week at 1000 °C, carefully x-rayed to confirm that it contained only V_2O_3 and the

metallic phase, and then analyzed to determine the mole fraction of vanadium in the alloy phase. It was subsequently examined with the galvanic cell method to determine the excess partial molar free energy of vanadium at very dilute concentrations. The technique, and the actual cell used in this experiment, are described in Section 2.

Before performing the experiment with the sample of unknown thermodynamic properties, the performance of the apparatus was checked with a cell of known potential. This cell consisted of a $VO-V_2O_3$ working electrode and a $Ta-Ta_2O_5$ reference electrode. The electrolyte was yittria-doped thoria. The EMF was measured at three different temperatures with each temperature repeated twice. The EMF versus temperature data obtained are tabulated below.

The data indicate that the EMF remained almost constant with temperature in agreement with the small variations of EMF with temperature obtained from thermodynamic calculations. The EMF value obtained at 1065 °C is slightly higher that the value obtained by R. Tetot.[14] This is a positive result because poor cell performances generally yield lower EMF's.

Cell 1 $Pt/VO-V_2O_3|Y_2O_3-ThO_2|Ta-Ta_2O_5|Pt$

T (°C)	EMF (mV)	R. Tetot et al.
975	81.0 ±0.5 mV	
975	80.2 ±0.5 mV	
1020	80.9 ±0.5 mV	
1020	80.0 ±0.5 mV	
1065	>81.9	
1065	79.8 ±0.5	73.0

The galvanic cell data for the V-Pd (X_V = 0.013) sample are listed below.

Cell 2 Pt|V_2O_3-Pd(V) (x_V = 0.013)|Y_2O_3-ThO_2|Ta-Ta_2O_5|Pt

Temp (°C)	EMF	Activity of V	$-\Delta G^o/R$
878	781	4.19×10^{-11}	0.298
973	777	2.76×10^{-10}	0.275
997	772	5.2085×10^{-10}	0.270
1021	771	8.0916×10^{-10}	0.264
1069	771	1.7082×10^{-9}	0.251

The EMF decreases slightly with temperature. The time required for this cell to initially reach equilibrium was approximately 80 h. The duration of the EMF measurements at each temperature was 8 h for temperatures below 1000 °C and 6 h for temperatures above 1000 °C. Measurements of each temperature were repeated at least twice. Once equilibrium was reached at a particular temperature the EMF remain almost constant for several hours. Fluctuations of the order of 1 mV were occasionally observed. A plot of EMF versus temperature (Fig. 3.9) illustrates the good performance of this cell. The EMF was invariant to the inert gas flow rates. Shorting of the electrodes with a 12 V battery for several minutes caused a large drop in the voltage of the cell. Fortunately, the EMF returned to its original values in a few hours. All of the above observations indicate that this was a good run. The activity coefficient calculated from this run is 2.31×10^{-8} at 100 °C ±20°C ($-\log\gamma$ = 7.70).

C. Summary

The activity coefficient of vanadium versus mole fraction is plotted in Fig. 3.9 for the vanadium-palldium system at 1000 °C. Although more data are needed to complete this plot, a large decrease of the activity with the mole fraction decreasing is observed. The vanadium activity coefficient is 10^{-8} at very low V concentrations. However, as the vanadium concentration increases to 40 at. % the activity coefficient rises to 1.35×10^{-2}, and finally, to 2.8×10^{-1} when the V concentration is 84 at. %. The activity coefficient has increased by seven orders of magnitude across the range of V concentration. This behavior indicates that the palladium forms very strong bonds across its homogeneous range with vanadium. A possible explanation of the data indicates that there is a large crystal field effect on the Pd 5-d orbitals. This effect greatly reduces the basicity of the more localized d orbital of Pd so that at high concentrations its most extended electron pairs are used. However, at high vanadium concentrations, pairs in more contracted orbitals are being used. This results in a large increase in activity coefficient. Such solution behavior is certainly different from that expected for an ideal solution in which the activity coefficient is unity.

The crystal field effect on the Pd orbitals is also illustrated by comparing the activity coefficients of vanadium in Pd and vanadium in Rh. The activity coefficient for rhodium was obtained only at high vanadium activities with oxide equilibria. In the VO-V_2O_3 region the activity coefficient of V in rhodium was measured to be 1.12×10^{-2} compared with that in Pd of 1.35×10^{-2}. At lower V activities, in the V_2O_3-VO_2 region, preliminary experiments showed that the activity

coefficient of V in Rh is greater than 10^{-8}. No detectable amounts of V were found to dissolve in Rh. These findings imply that rhodium is a better base than Pd at high vanadium activities, but it may be inferior at low vanadium activities. This can be explained in terms of crystal field effects. A d orbital of palladium would be more localized than a comparable d orbital of rhodium because of the higher Pd nuclear charge. However, Pd has one more nonbonding electron pair than rhodium which can be donated in an acid-base reaction. At low vanadium concentrations (low V activity) Pd would be using its most extended pair. When this is consumed, more localized pairs that occupy an orbital comparable to that occupied by the nonbonding pair of rhodium would be used and the basicity of Pd would be inferior to that of rhodium.

In agreement with the predictions of the acid-base theory, the acidity increases upon moving down the Periodic Table from rhodium to iridium. The activity coefficient of vanadium in iridium in the VO-V_2O_3 region is 8.32×10^{-3} while that of rhodium is 1.12×10^{-2}. Clearly, Ir is a better base than rhodium because the 5d orbitals of Ir are more extended that the 4d orbitals of Rh. Iridium is also a better base than Pd at higher vanadium activities. In the V_2O_3-V_3O_5 region the activity coefficient of vanadium in Ir is 4.27×10^{-10} while that in Pd is larger by approximately an order of magnitude ($\gamma_V = 4.78 \times 10^{-9}$). In the VO-$V_2O_3$ region the activity coefficient of V in Pd is larger by 60%, while at high V activity (V_2O-V_4O region) the coefficients are almost equal. Although iridium has one less nonbonding pair than palladium, it has greater base capacity at lower vanadium concentrations because this pair occupies a 5d orbital that is more extended than the 4d orbital of Pd.

At high vanadium concentrations the activity coefficients of V in Ir and Pd are almost equal because Ir has fewer pairs that does Pd. Also in agreement with the acid-base theory are the results obtained for the Nb-Ir system when compared to the Nb-Pd system studied by Cima. The activity coefficient of Nb in Ir (in the $NbO-NbO_2$ region) is 3.85×10^{-2}, while that in Pd is 5.49×10^{-2}, confirming that Ir is a better base than Pd.

The data obtained for the Ti-Ir alloys when compared with those of the V-Ir system will be useful in describing the difference in acid-base reactions in which two vacant orbitals are involved. Also the data obtained for Nb-Ir alloys compared with the V-Ir data will be used to characterize the acid-base reaction when acids that have the same number of vacant orbitals but belong to different quantum shells are involved. The preliminary data obtained in this study is part of a continuing effort to develop a quantitative model that will be used to predict thermodynamic stabilities of intermetallics. The results are consistent with the Lewis acid-base model applied to transition metal intermetallics. Present work is concentrated on the completion of the acid-base titration curves of vanadium with the platinum group metals to completely resolve the behavior of acid-base reactions in these systems.

IV. REFERENCES

1. H. Endo, M. Wakinara, M. Taniguchi and T. Katsura, Bull. Chem. Soc. Jpn **46**, 2087-90 (1973).
2. R. P. Elliot, **Constitution of Binary Alloys**, First Suppl., p. 703, McGraw-Hill, New York, 1965.
3. W. Koster, W. D. Haehl, Z. Metallk. **49**, 647-49 (1958).

4. R. M. Waterstrat, J. Less-Common Metals **80**, 31-66 (1981).

5. R. M. Waterstrat, R. C. Manuszewski, J. Less-Common Metals **52**, 293-305 (1977).

6. J. F. Smith, J. Alloy Phase Diagrams 3(3), 143-47 (1987).

7. R. M. Waterstrat, Metall. Trans. 4, 455 (1973).

8. B. C. Giesen, P. N. Dangel and N. J. Grant, J. Less-Common Metals **13**, 62 (1967).

9. R. P. Elliot, **Constitution of Binary Alloys**, First Suppl., p. 293, McGraw-Hill, New York, 1965.

10. **Binary Alloy Phase Diagrams**, T. B. Massalski, ed., Vol. 2, p. 1423, American Society for Metals, Metals Park, Ohio, 1986.

11. B. T. Matthias, V. B. compton and E. Corenzwit, Phys. Chem. Solids **19**, 130-33 (1961).

12. A. L. Gray, R. Kershaw, W. Croft, K. Dwight and A. Wold, J. Solid State Chem. **62**, 57-62 (1986).

13. M. J. Cima, Ph.D. dissertation, University of Calif., Berkeley, 1986.

14. R. Tetot and C. Picard, J. Solid State Chem. **66**, 324 (1987).

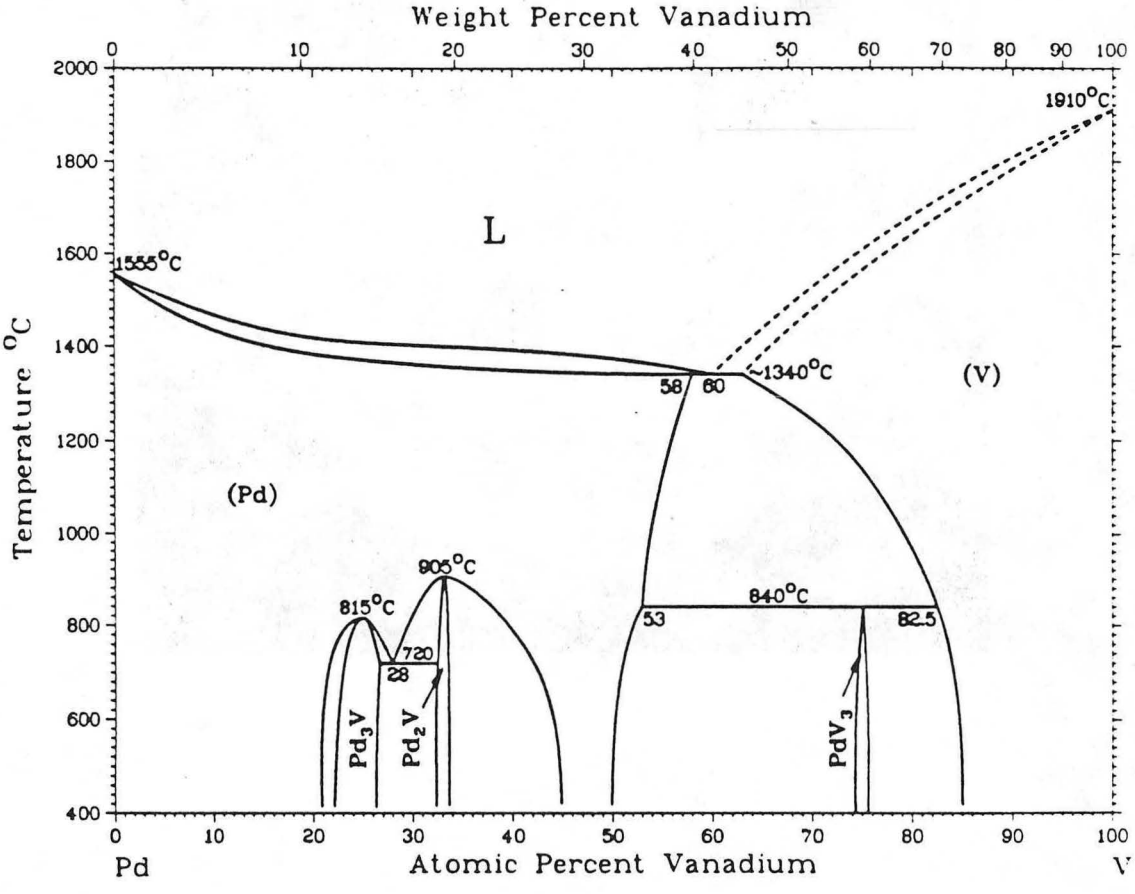

FIG. 3.1. The vanadium-palladium phase diagram as determined by W. Köster et al.

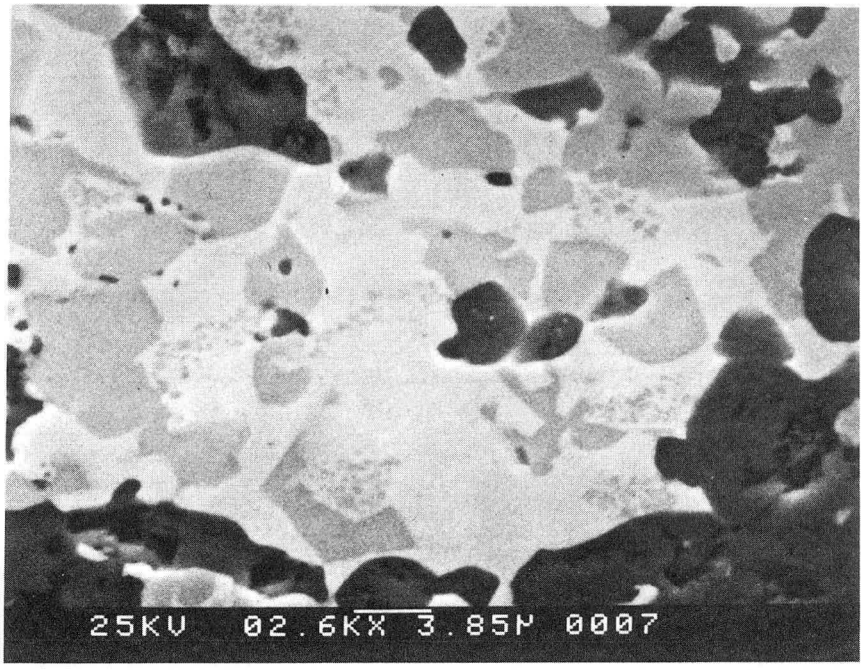

FIG. 3.2. Scanning electron micrograph of VPd6. The two metallic grains belong to the V_3Pd ordered phase and a Pd(V) solid solution. The darker grains belong to VO.

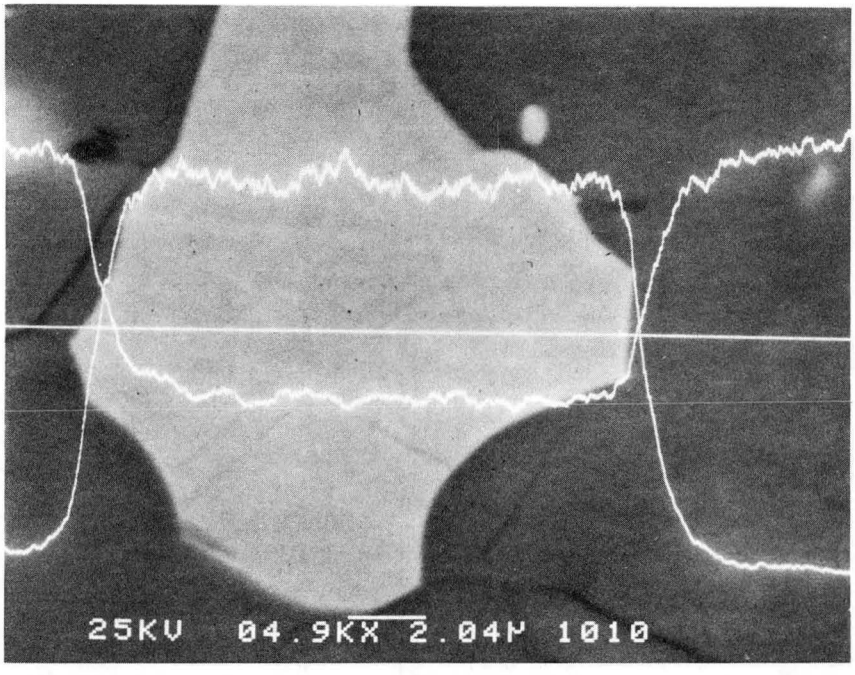

FIG. 3.3 Scanning electron micrograph of VPd7. The palladium and the vanadium L(α) x-ray intensity tracings are the top and bottom lines, respectively. They are taken along the solid white line across the center of the alloy grain.

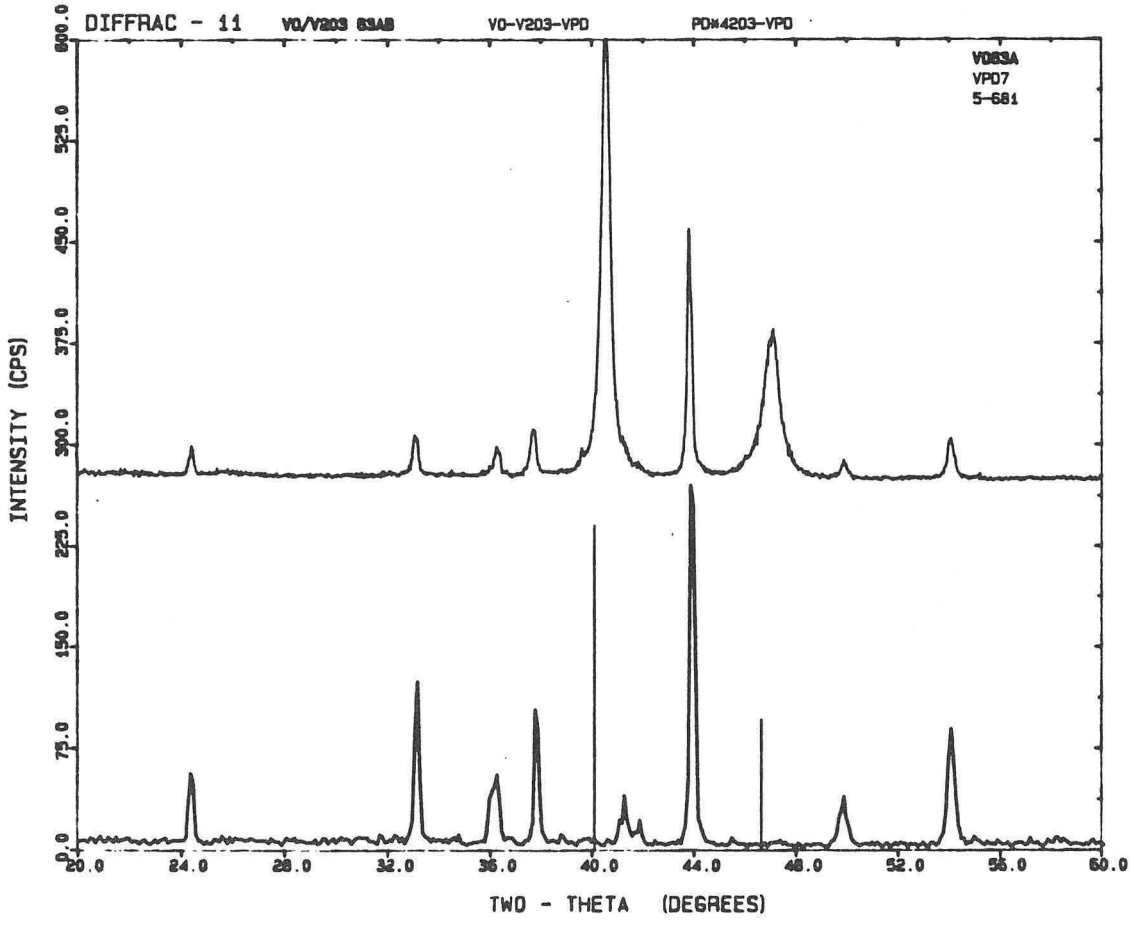

FIG. 3.4. X-ray diffraction pattern of VPd7. The lower pattern is from a sample containing VO, V_2O_3 and the simulated pattern of Pd metal (lines).

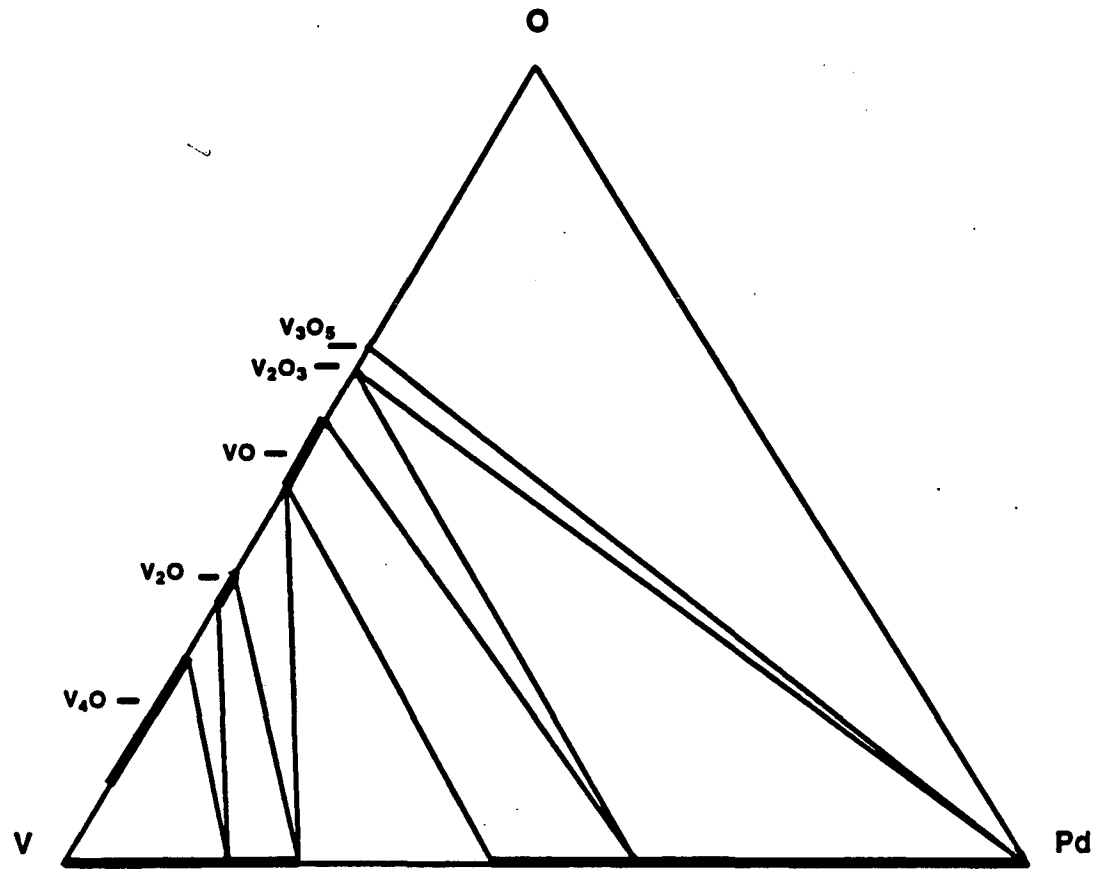

FIG. 3.5. The V-Pd-O phase diagram at 1050 °C. It consists only of multiphase regions of binary phases.

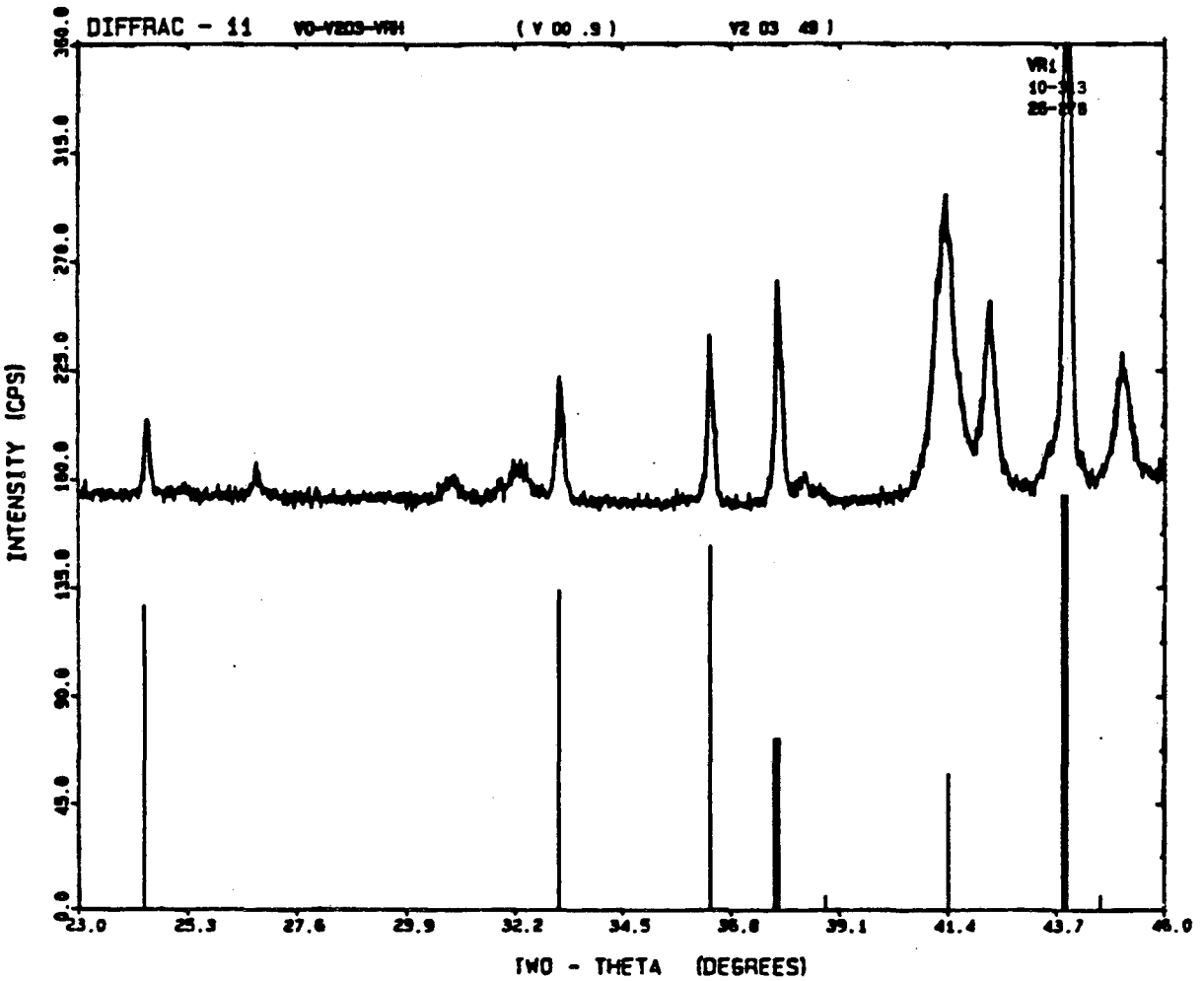

FIG. 3.6. X-ray diffraction pattern of VR1. It is compared with the simulated patterns of VO (broad lines) and V_2O_3 (thin lines). The remaining reflections belong to the α_3-VRh phase. The crystalographic data for this phase are listed in Table 3.2.

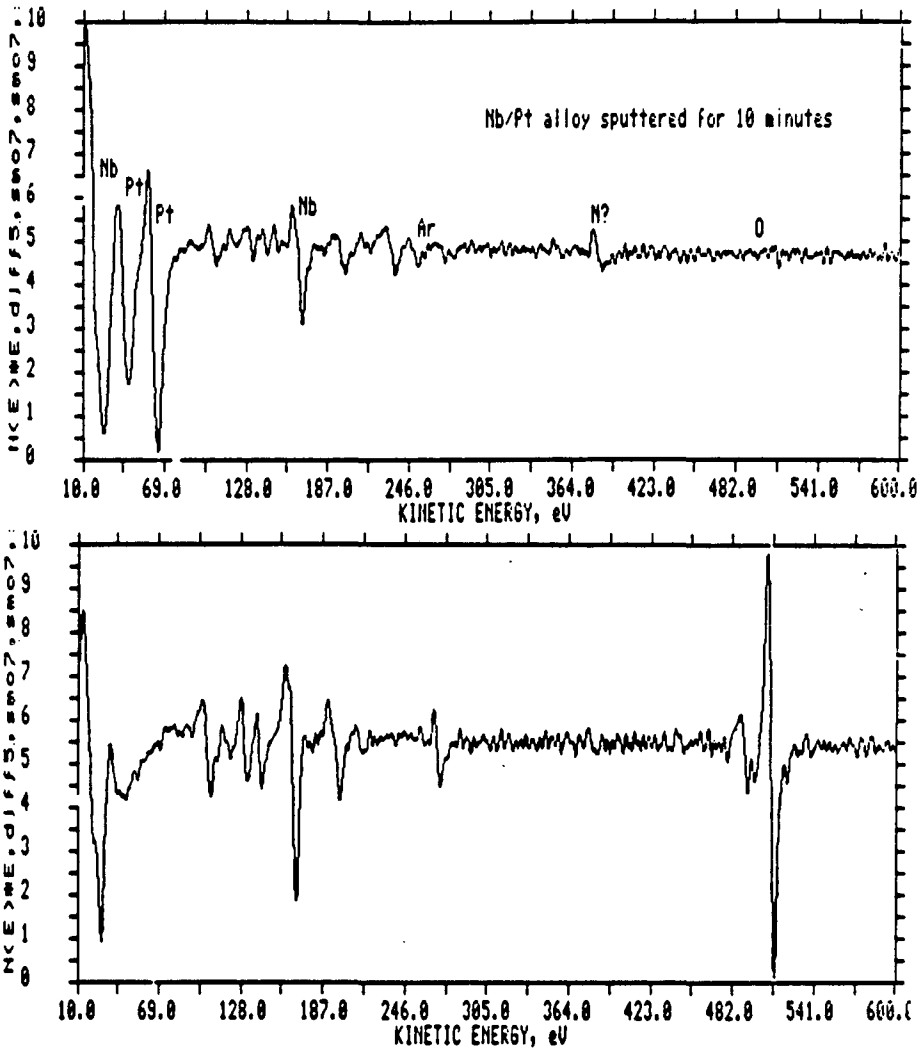

FIG. 3.7. The Auger electron energy derivative spectra for an alloy grain (top) and an oxide grain (bottom) of a Nb-Pt-O sample. The spectrum of the alloy grain was obtained after the sample was ion-bombarded for 10 min. The spectrum of the oxide was obtained on a pristine surface. The absence of Pd in the oxide grain and the absence of oxygen in the alloy grain is clearly illustrated in the above spectra.

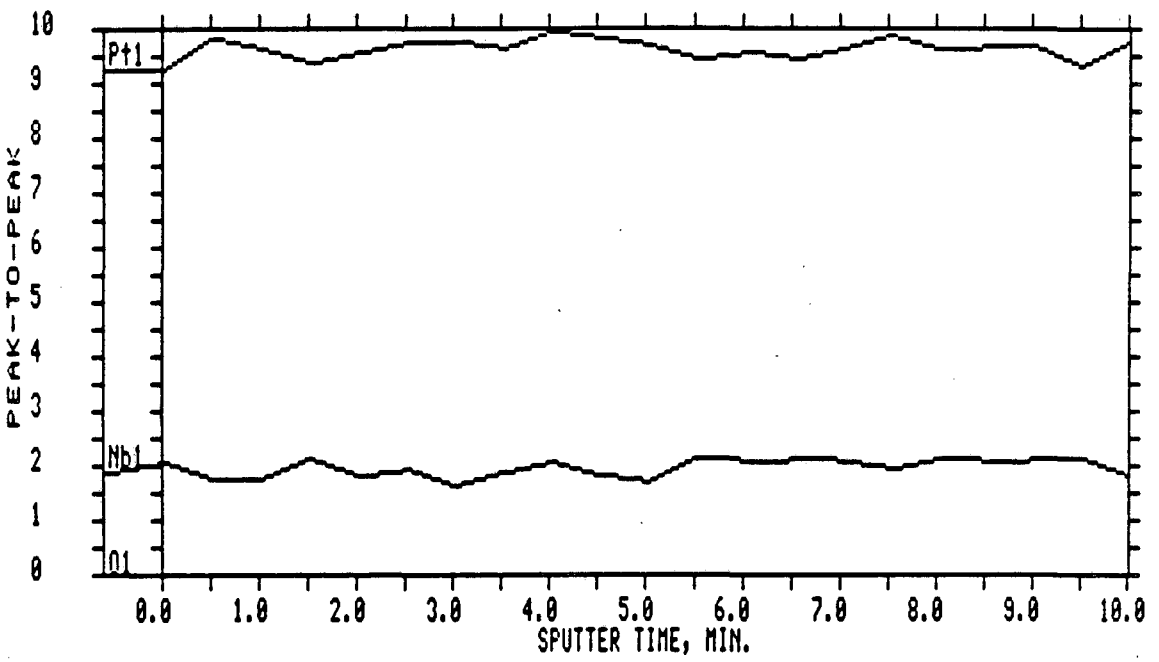

FIG. 3.8. The composition versus depth profile for the Nb-Pd grain.

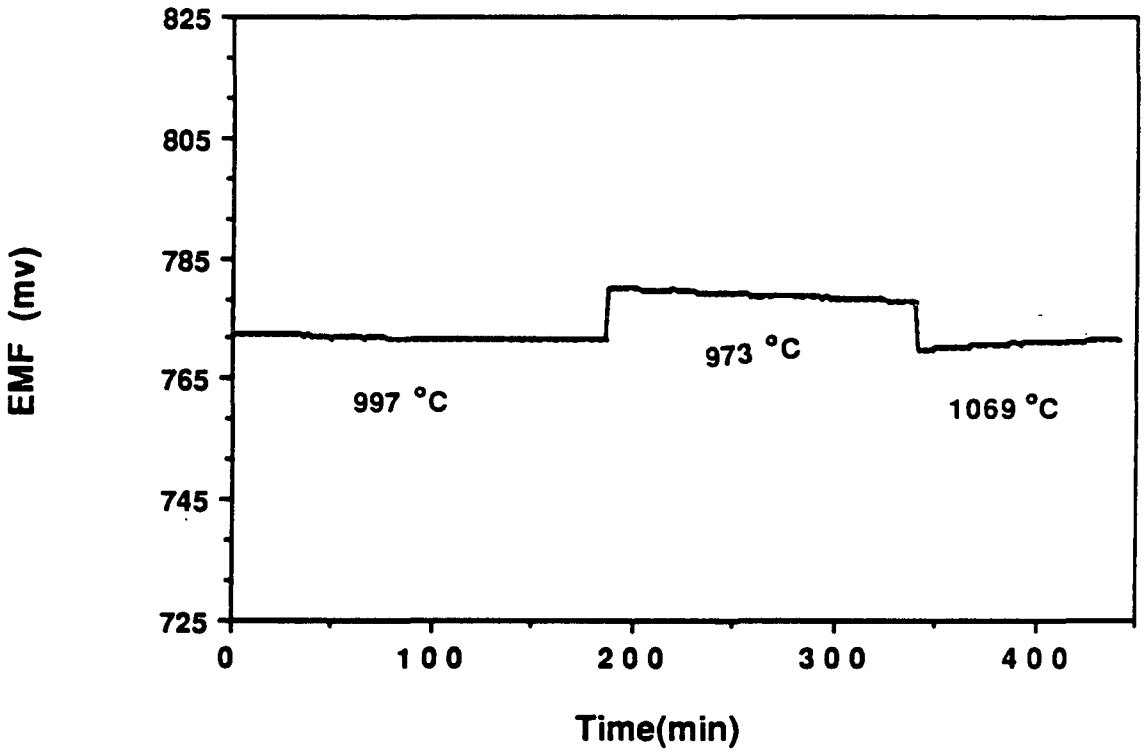

FIG. 3.9. The performance of the cell Ta-Ta_2O_5/YDT/Pd(V)V_2O_3 (sample VPd15). This is a plot of EMF versus time and temperature.

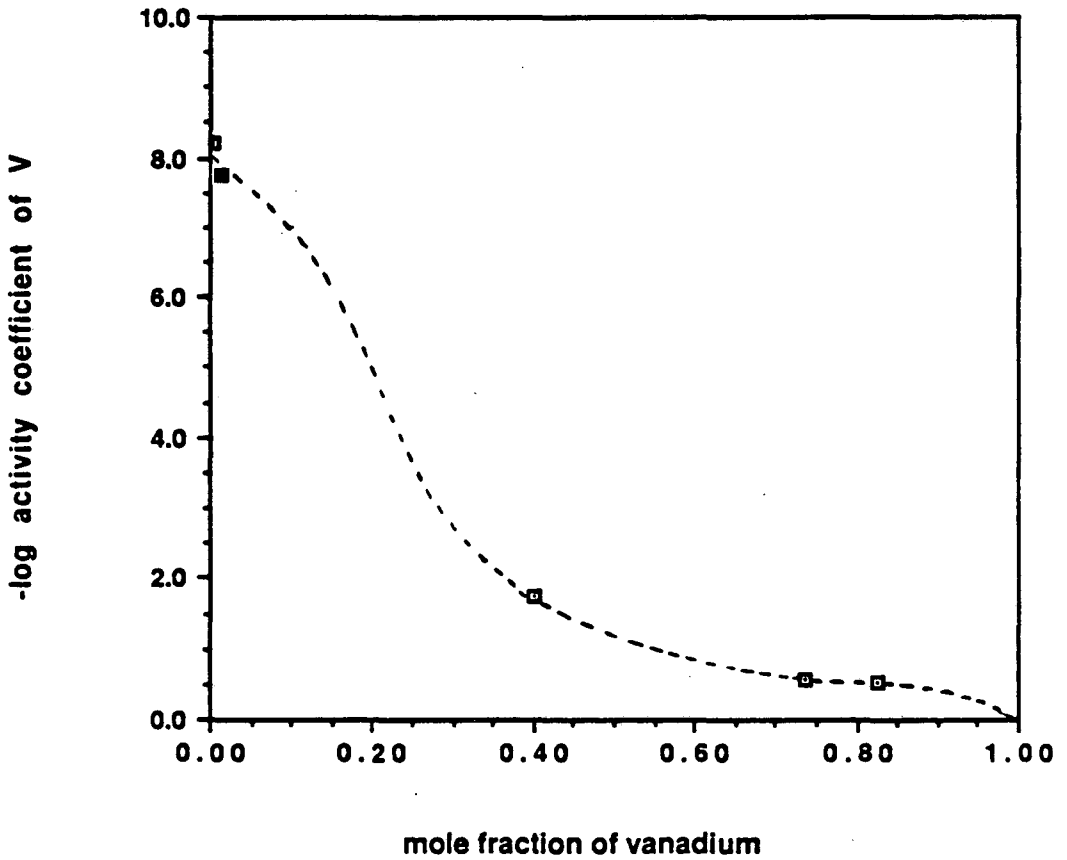

FIG. 3.10. The vanadium-palladium partial titration curve at 1000 °C. The point obtained from the galvanic cell measurement is the filled square.

TABLE 3.1. Summary of preparation of V-Pd-O samples

Sample ID	Reaction temp. Hot-pressing	Annealing conditions	% Weight change
VPd1	1175 °C	17 days 1000 °C	0.06
VPd2	1250 °C	21 days 1050 °C	-0.40
VPd3	1150 °C	11 days 1050 °C	-0.48
VPd4	1150 °C	17 days 1000 °C	-0.13
VPd5	1100 °C	11 days 1000 °C	-0.49
VPd6	1150 °C	14 days 1050 °C	-0.26
VPd7	1100 °C	2 days 800 °C	-0.30
		10 days 1000 °C	
VPd8	1100 °C	17 days 1000 °C	0.26
VPd9	1050 °C	7 days 1000 °C	--
VPd10	1000 °C	7 days 1050 °C	-0.80
VPd11	1000 °C	7 days 1050 °C	-1.20
VPd12	1000 °C	10 days 1000 °C	-0.72
VPd13	1000 °C	10 days 1050 °C	-2.0
VPd14	1150 °C	7 days 1050 °C	-4.60
VPd15	1150 °C	2 days 800 °C	0.0
		11 days 1000 °C	

TABLE 3.2 Results for vanadium-palladium oxide equilibria.

Sample ID	Reactants	Alloy Composition Xv	Equilibrium Phases
VPd1	V_2O_3, V, Pd	0.855	V_4O, $V_{s.s.}$
VPd2	V_2O_3, V, Pd	0.825	V_4O_2, V_2O, $V_{s.s.}$
VPd3	V_2O_3, V. Pd	0.830	V_4O, V_2O, $V_{s.s.}$
VPd4	V_2O_3, V, Pd	0.770	V_2O, $V_{s.s.}$
VPd5	V_2O_3, V, Pd	0.740	V_2O, $VO_{0.8}$, $V_{s.s.}$
VPd6	$VO_{0.9}$, V, Pd	0.590	$VO_{0.8}$, $V_{s.s.}$
		0.740	
VPd7	V_2O_3, V, Pd	0.395	$VO_{1.2}$, V_2O_3
VPd8	VO, V_2O_3, V, Pd	0.385	$VO_{1.2}$, V_2O_3
VPd9	VO, V_2O_3, Pd	0.331	V_2O_3, $Pd_{s.s.}$
VPd10	V_2O_3, Pd	0.006	V_2O_3, V_3O_5, $Pd_{s.s.}$
VPd11	V_2O_3, V_3O_5, V, Pd	0.005	V_2O_3, V_3O_5, $Pd_{s.s.}$
VPd12	V_2O_3, VO_2	--	V_3O_5, V_4O_7, Pd
VPd13	$VO_{1.8}$, Pd	--	$VO_{1.8}$, $Pd_{s.s.}$
*VPd14	V_2O_3, V, Pd	0.110	V_2O_3, $Pd_{s.s.}$
*VPd15	V_2O_3, V, Pd	0.013	V_2O_3, $Pd_{s.s.}$

*Electrodes for the electrochemical system.

TABLE 3.3. Relative intensities (I), interplanar spacing (d) and crystallographic angle (2θ) of the α_3-phase reflections.

	α_3-VRh		
hkl	d	2θ	I
020	3.33	26.71	W
200	2.89	30.89	W
001	2.77	32.20	W
111	2.34	38.37	W
220	2.18	41.28	S
021	2.14	42.26	M
130	2.08	43.40	W
201	2.01	45.00	M

TABLE 3.4. Summary of preparation of V-Rh-O and V-Ir-O samples.

Sample ID	Reactants	Reaction temp. hot-pressing	Annealing conditions	% Weight change
VR1	VO, V_2O_3, Rh	1200 °C	1 wk 1200 °C	-0.10
VR2	V_2O_3, V, Rh	1175 °C	1 wk 1300 °C	-0.10
			2 wk 1050 °C	
VR3	V_2O_3, V, Rh	1175 °C	1 wk 1300 °C	-0.20
			2 wk 1050 °C	
VR4	V_2O_3, V, Rh	1175 °C	2 wk 1050 °C	
VI1	V_2O_3, V, Ir	1250 °C	1 wk 1300 °C	-0.03
			2 wk 1000 °C	
VI2	V_2O_3, V, Ir	1250 °C	1 wk 1300 °C	-0.06
			2 wk 1000 °C	
VI3	V_2O_3, V, Ir	1300 °C	1 wk 1300 °C	-0.03
			2 wk 1000 °C	
VI4	V_2O_3, V, Ir	1300 °C	1 wk 1300 °C	-0.03
			2 wk 1000 °C	
VI5	V_2O_3, V_3O_5, Ir	1325 °C	1 wk 1300 °C	-0.26
			2 wk 1000 °C	
VI6	V_2O_3, Ir	1300 °C	3 wk 1000 °C	0.03
VI7	V_2O_3, VO, Ir	1250 °C	4 wk 1050 °C	-1.20

TABLE 3.5a. Results for V-Rh-O equilibria.

Sample ID	Reactants	Products	Alloy Composition at% V	at% Rh
VR1	VO, V_2O_3, Rh	VO, V_2O_3, RhV	48.0	52.0
VR2	V_2O_3, V, Rh	V_4O, V_2O, V(Rh)	88.0	12.0
VR3	V_2O_3, V, Rh	V_2O, VO, V(Rh)	84.5	15.5
VR4	V_2O_3, V, Rh	V_2O, VO, V(Rh)		

TABLE 3.5b. Results for V-Ir-O equilibria.

Sample ID	Reactants	Products	Rv	Alloy Composition at% V	at% Ir
VI1	V_2O_3, V, Ir	V_2O_3, IrV, IrV_3	0.762	53.20	46.80
VI2	V_2O_3, V, Ir	V_2O_3, IrV_3			
VI3	V_2O_3, V, Ir	V_2O, VO, IrV_3	0.773	75.10	24.91
VI4	V_2O_3, V, Ir	V_2O, IrV_3, V	0.814	78.35	21.64
VI5	V_3O_5, V_2O_3, Ir	V_2O_3, (V_3O_5), Ir(V)	0.094	8.81	91.19
VI6	V_3O_5, Ir	V_2O_3, (V_3O_5), Ir(V)	0.083	8.10	91.55
VI7	V_2O_3, VO, Ir	VO, V_2O_3, Ir(V)	0.584	65.30	34.70

TABLE 3.6. Summary of preparation Nb-Ir-O, Nb-Pt-O and Ti-Ir-O samples.

Sample ID	Reactants	Reaction temp. Hot-pressing	Annealing conditions	% Weight change
NbI1	NbO, Ir	1200 °C	7 days 1400 °C	-0.23
NbPt1	NbO, Nb, Pt	1250 °C	7 days 1400 °C	-0.13
NbPt2	NbO, Nb, Pt	1200 °C	5 days 1400 °C	-0.501
NbPt3	Nb_2O_5, Nb, Pt	1000 °C	5 days 1400 °C	--
TiI1	Ti_2O_3, Ir	1300 °C	4 days 1400 °C	+0.47
TiI2	Ti_2O_3, Ti, Ir	1300 °C	4 days 1400 °C	-5.0

TABLE 3.7. Results for the NbIr, NbPt and NbTi samples.

Sample ID	Products	Rv	Alloy Composition at% Nb,Ti	at% Ir,Pt
NbI1	NbO, NbO_2 σ-Nb-Ir	0.167	33.74	66.26
NbPt1	NbO, NbO_2	--		
NbPt2	--	--		
NbPt3	$Nb_{12}O_{29}$, $NbO_{0.45}$, $NbPt_3$	--	25.0 ±1	75.0 ±1
TiI1	TiO, Ti_2O_3, IrTi	0.581	47.0	53.0
TiI2	Ti_2O_3, Ti_3O_5, Ir_3Ti	0.340	24.9	75.1

LAWRENCE BERKELEY LABORATORY
TECHNICAL INFORMATION DEPARTMENT
UNIVERSITY OF CALIFORNIA
BERKELEY, CALIFORNIA 94720